Journal of the Mechanics and Physics of Solids 86 (2016) 150–172

Contents lists available at ScienceDirect

Journal of the Mechanics and Physics of Solids

journal homepage: www.elsevier.com/locate/jmps

A multi-scale modeling framework for instabilities of film/substrate systems

Fan Xu [a,b,*], Michel Potier-Ferry [a]

[a] Laboratoire d'Etude des Microstructures et de Mécanique des Matériaux, LEM3, UMR CNRS 7239, Université de Lorraine, Ile du Saulcy, 57045 Metz Cedex 01, France

[b] Department of Mechanics and Engineering Science, Fudan University, 220 Handan Road, 200433 Shanghai, PR China

ARTICLE INFO

Article history:
Received 8 July 2015
Received in revised form
19 August 2015
Accepted 12 October 2015
Available online 23 October 2015

Keywords:
Wrinkling
Post-buckling
Multi-scale
Fourier series
Path-following technique
Finite element method

ABSTRACT

Spatial pattern formation in stiff thin films on soft substrates is investigated from a multi-scale point of view based on a technique of slowly varying Fourier coefficients. A general macroscopic modeling framework is developed and then a simplified macroscopic model is derived. The model incorporates Asymptotic Numerical Method (ANM) as a robust path-following technique to trace the post-buckling evolution path and to predict secondary bifurcations. The proposed multi-scale finite element framework allows sinusoidal and square checkerboard patterns as well as their bifurcation portraits to be described from a quantitative standpoint. Moreover, it provides an efficient way to compute large-scale instability problems with a significant reduction of computational cost compared to full models.

1. Introduction

In nature, surface morphological instabilities of a stiff thin layer attached on a soft substrate have been widely observed such as wrinkles of hornbeam leaf and human skin, and these phenomena have raised considerable research interests over the last decade (Efimenko et al., 2005; Mahadevan and Rica, 2005; Stoop et al., 2015). In modern industry, surface wrinkles can be widely applied in large area ranging from the micro/nano-fabrication of flexible electronic devices with controlled morphological patterns (Bowden et al., 1998; Rogers et al., 2010), the design of coated materials or living tissues (Brau et al., 2011), to the mechanical property measurement of material characteristics (Howarter and Stafford, 2010). Several theoretical, numerical and experimental works have been devoted to stability analyses in order to determine the critical conditions of instability and the corresponding wrinkling patterns (Audoly and Boudaoud, 2008a,b,c;Chen and Hutchinson, 2004; Huang and Im, 2006; Huang et al., 2005; Song et al., 2008). In particular, there are several analytical solutions of models linearized from homogeneous finite deformation, in the case of half-spaces (Dowaikh and Ogden, 1990; Hayes and Rivlin, 1961; Shield et al., 1994) and film/substrate systems (Cai and Fu, 1999, 2000; Steigmann and Ogden, 1997). During post-buckling, the amplitude and wavelength of wrinkles will vary with respect to externally applied compressive load. Due to its well-known difficulty, most recent post-buckling analyses have recourse to numerical approaches since only a limited number of exact analytical solutions can be obtained in very simple or simplified cases. In most of early numerical studies,

* Corresponding author at: Laboratoire d'Etude des Microstructures et de Mécanique des Matériaux, LEM3, UMR CNRS 7239, Université de Lorraine, Ile du Saulcy, 57045 Metz Cedex 01, France.
E-mail address: fan.xu@univ-lorraine.fr (F. Xu).

http://dx.doi.org/10.1016/j.jmps.2015.10.003
0022-5096/

the 2D or 3D spatial problem of film/substrate is often discretized by either spectral method or Fast Fourier Transform (FFT) algorithm, which is fairly computationally inexpensive but prescribes periodic boundary conditions and simple geometries. Recent efforts have been devoted to 2D or 3D numerical study of film/substrate buckling by using finite element method (Cai et al., 2011;Cao and Hutchinson, 2012a,b;Cao et al., 2012; Stoop et al., 2015; Sun et al., 2012; Xu et al., 2014b, 2015a,b; Zang et al., 2012), which is more computationally expensive but more flexible to describe complex geometries and general boundary conditions, and also allows using commercial computer codes.

The previous works of Xu (2014) and Xu et al. (2014a,b, 2015a,b) proposed a whole numerical framework to study surface wrinkling of thin films bound to compliant substrates, through applying advanced numerical methods for bifurcation analyses and focusing on the post-buckling evolution involving multiple bifurcations, which for the first time addressed the post-bifurcation response of film/substrate systems from a quantitative standpoint. In this framework, the emergence and post-buckling evolution of several typical 2D or 3D wrinkling modes like sinusoidal, period-doubling, checkerboard and herringbone were thoroughly investigated (Xu et al., 2014b, 2015a,b). In addition, the effects of a large range of stiffness ratio E_f/E_s from $O(1)$ to $O(10^5)$ on instability patterns and the choices of different modeling frameworks, i.e. small strain linear elasticity or finite strain hyperelasticity, were deeply discussed. In these cases, the spatial shape of system responses looks like a slowly modulated oscillation and direct simulation of such cellular instabilities in a big sample often requires numerous degrees of freedom. Therefore, from the computational point of view, it would be interesting and important to develop reduced-order models to dramatically cut the computational cost and time, and to be able to simulate a large number of wrinkles.

A multi-scale approach based on the concept of Fourier series with slowly varying coefficients has been developed to study the instabilities with nearly periodic patterns (Damil and Potier-Ferry, 2006, 2008, 2010). It has been successively applied to the buckling of a long beam lying on a nonlinear elastic foundation (Mhada et al., 2012; Xu et al., 2014a), global and local instability interaction of sandwich structures (Liu et al., 2012; Mhada et al., 2013), and membrane wrinkling (Damil et al., 2013, 2014). This multi-scale approach is based on the Ginzburg–Landau theory (Iooss et al., 1989; Wesfreid and Zaleski, 1984). In the proposed theory, the envelope equation is derived from a double-scale analysis and the nearly periodic fields (reduced-order models) are represented by Fourier series with slowly varying coefficients. This mathematical representation yields macroscopic models in the form of generalized continua. In this technique, the macroscopic field is defined by Fourier coefficients of the microscopic field. It has been established that the models obtained in this way are consistent with the Ginzburg–Landau technique, but can remain valid away from the bifurcation (Damil and Potier-Ferry, 2010).

This work aims at building a multi-scale reduced modeling framework based on this Fourier-related technique to study the occurrence and evolution of film/substrate instability phenomena. A general macroscopic modeling framework will be derived first, which can be directly used for any 3D film/substrate discretization at the expense of computational cost and flexibility. Then a simplified 3D macroscopic model will be proposed by taking into account the property of film thinness, through associating a nonlinear macroscopic plate model representing the film and a linear macroscopic elasticity describing the substrate. The model incorporates Asymptotic Numerical Method (ANM) (Cochelin, 1994; Cochelin et al., 1994, 2007; Damil and Potier-Ferry, 1990) as a robust path-following technique to predict secondary bifurcations on their post-buckling evolution path as the load is increased. The tracing of post-bifurcation response is an important but difficult numerical problem. The ANM gives interactive access to semi-analytical equilibrium branches, which offers considerable advantage of reliability compared to classical iterative algorithms. By taking advantage of the local polynomial approximations of the branch within each step, the algorithm is remarkably robust and fully automatic. Furthermore, unlike incremental-iterative methods, the arc-length step size in the ANM is fully adaptive since it is determined *a posteriori* by the algorithm. A small radius of convergence and step accumulation appear around a bifurcation point and imply its presence.

This paper investigates the appearance and post-buckling evolution of instability patterns of 3D film/substrate systems, for the first time starting from a multi-scale standpoint. The paper is organized as follows. In Section 2, a generalized macroscopic modeling framework is presented first. Then in Section 3, a simplified 3D macroscopic model is derived, which couples a nonlinear macroscopic plate model to represent the film and a macroscopic linear elastic solid to describe the substrate. The resulting nonlinear problem is then reformulated by the ANM algorithm as a path-following technique in Section 4. Results and discussions are provided in Section 5, including the onset and evolution of sinusoidal wrinkles, square checkerboard patterns and alternating packets of large and small amplitude undulations. Conclusions and perspectives are reported in Section 6.

2. General macroscopic modeling framework

We will conduct a multi-scale approach based on the concept of Fourier series with slowly varying coefficients. Let us suppose that the instability wave number q is known. In this way, all the unknowns of model $U(x) = \{u(x), s(x), \gamma(x), \ldots\}$ can be written in the form of Fourier series, whose coefficients vary more slowly than the harmonics:

$$U(x) = \sum_{j=-\infty}^{+\infty} U_j(x) e^{jiqx}, \tag{1}$$

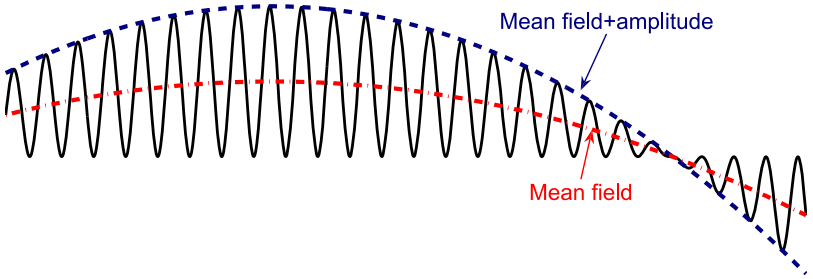

Fig. 1. At least two macroscopic fields (the mean field and the amplitude of the fluctuation) are necessary to describe a nearly periodic response.

where the Fourier coefficient $U_j(x)$ denotes the envelope for the jth order harmonic, which is conjugated with $U_{-j}(x)$.

The macroscopic unknown fields $U_j(x)$ slowly vary over a period $[x, x+\frac{2\pi}{q}]$ of the oscillation. In practice, only a finite number of Fourier coefficients will be considered. As shown in Fig. 1, at least two functions $U_0(x)$ and $U_1(x)$ are necessary to describe nearly periodic patterns: $U_0(x)$ can be identified with the mean value while $U_1(x)$ represents the envelope or amplitude of the spatial oscillations. The mean value $U_0(x)$ is real valued, while the other envelopes are complex. Consequently, the envelope of the first harmonic $U_1(x)$ can be written as $U_1(x) = r(x)e^{i\varphi(x)}$, where $r(x)$ represents the amplitude modulation and $\varphi(x)$ is the phase modulation. If the phase varies linearly like $\varphi(x) = Qx + \varphi_0$, this type of approach is able to describe quasi-periodic responses whose wave number $q + Q$ slightly differs from the *a priori* chosen q. Hence, the method makes it possible to account for a small change in wave number.

The main idea of the Fourier-related macroscopic modeling is to deduce differential equations satisfied by the amplitude $U_j(x)$. Some calculation rules have been introduced in Damil and Potier-Ferry (2006, 2010) to manage these Fourier series with slowly varying coefficients. Derivative operators can be calculated exactly. If a univariate scalar function $a(x)$ is in the form (1), the Fourier coefficients of its derivatives are given by

$$\left(\frac{\mathrm{d}a}{\mathrm{d}x}\right)_j = (a')_j = \left(\frac{\mathrm{d}}{\mathrm{d}x} + jiq\right)a_j = (a_j)' + jiqa_j, \tag{2}$$

$$\left(\frac{\mathrm{d}^2a}{\mathrm{d}x^2}\right)_j = (a'')_j = \left(\frac{\mathrm{d}}{\mathrm{d}x} + jiq\right)^2 a_j = (a_j)'' + 2jiq(a_j)' - j^2q^2a_j. \tag{3}$$

The second rule concerns the product of two functions $a(x)$ and $b(x)$ in the form (1). A basic identification of Fourier coefficients leads to

$$(ab)_j = \sum_{j_1=-\infty}^{+\infty} a_{j_1}b_{j-j_1}. \tag{4}$$

The above Fourier-related methodology has been applied to various mechanical models. For the sake of illustration, let us discuss a nonlinear elasticity problem: the Saint–Venant Kirchhoff model based on a linear constitutive law between the second Piola–Kichhoff stress and the Green-Lagrange strain. The corresponding macroscopic model has been deduced in Damil and Potier-Ferry (2008) and then discretized in a finite element framework in Mhada et al. (2013). For simplicity, we only demonstrate the derivation of constitutive laws using the Fourier-related method. In the framework of linear constitutive laws, the second Piola–Kichhoff stress $\{s\}$ and the Green–Lagrange strain $\{\gamma\}$ are linked linearly, while the strain is related to the displacement gradient $\{\theta\}$ by a quadratic relationship:

$$\begin{cases} \{s\} = [D]\{\gamma\}, \\ \{\gamma\} = [H]\{\theta\} + \frac{1}{2}[A(\theta)]\{\theta\}, \end{cases} \tag{5}$$

where the elastic matrix $[D]$, the linear matrix $[H]$, the quadratic matrix $[A(\theta)]$ and the displacement gradient vector $\{\theta\}$ are defined in Appendix A.

We seek nearly periodic responses that vary rapidly in one direction. This characteristic direction and the period are described by a wave vector $\mathbf{q} \in \mathbb{R}^3$ that is assumed as a given parameter. In practice, this vector can be obtained from linear stability analysis. Hence, the vector $\mathbf{U}(\mathbf{x})$ that includes displacement vector, its gradient, strain and stress tensors, is sought in the form of Fourier series, whose coefficients $\mathbf{U}_j(\mathbf{x})$ vary slowly. For simplicity, we keep up to the level two harmonics but higher level harmonics can be considered for complex wave oscillations:

$$\mathbf{U}(\mathbf{x}) = \sum_{j=-2}^{+2} \mathbf{U}_j(\mathbf{x}) e^{jiqx}. \tag{6}$$

After applying the rule (4) to the constitutive law (5), one can obtain a macroscopic constitutive law for harmonic 0 (real value) and two constitutive laws for harmonics 1 and 2 (complex values), with all these coupled equations:

$$\begin{cases} \{\gamma_0\} = \left[D\right]^{-1}\{s_0\} = \left[H\right]\{\theta_0\} + \frac{1}{2}\left[A(\theta_0)\right]\{\theta_0\} + \left[A(\theta_{-1})\right]\{\theta_1\} + \left[A(\theta_{-2})\right]\{\theta_2\}, \\ \{\gamma_1\} = \left[D\right]^{-1}\{s_1\} = \left[H\right]\{\theta_1\} + \left[A(\theta_0)\right]\{\theta_1\} + \left[A(\theta_{-1})\right]\{\theta_2\}, \\ \{\gamma_2\} = \left[D\right]^{-1}\{s_2\} = \left[H\right]\{\theta_2\} + \left[A(\theta_0)\right]\{\theta_2\} + \frac{1}{2}\left[A(\theta_1)\right]\{\theta_1\}. \end{cases} \tag{7}$$

Therefore, a generalized continuum model has been defined by superposition of several harmonics. Like each field in the model, the displacement is replaced by a generalized displacement that includes five Fourier coefficients for $j \in [-2, 2]$. To facilitate the understanding and implementation, the macroscopic constitutive law (7) can be unified in the same generic form as the starting law (5):

$$\begin{cases} \{S\} = \left[D^{gen}\right]\{\Gamma\}, \\ \{\Gamma\} = \left[H^{gen}\right]\{\Theta\} + \frac{1}{2}\left[A^{gen}(\Theta)\right]\{\Theta\}, \end{cases} \tag{8}$$

where the generalized stress $\{S\}$, the generalized strain $\{\Gamma\}$ and the generalized displacement gradient $\{\Theta\}$ also include five Fourier coefficients for $j \in [-2, 2]$:

$$\begin{cases} \{S\} = \{\{s_0\}, \{s_1^R\}, \{s_1^I\}, \{s_2^R\}, \{s_2^I\}\}, \\ \{\Gamma\} = \{\{\gamma_0\}, 2\{\gamma_1^R\}, 2\{\gamma_1^I\}, 2\{\gamma_2^R\}, 2\{\gamma_2^I\}\}, \\ \{\Theta\} = \{\{\theta_0\}, \{\theta_1^R\}, \{\theta_1^I\}, \{\theta_2^R\}, \{\theta_2^I\}\}, \end{cases} \tag{9}$$

where the superscripts R and I denote the real part and the imaginary part of complex numbers, respectively. The generalized matrices $[D^{gen}]$, $[H^{gen}]$ and $[A^{gen}(\Theta)]$ are detailed in Appendix A. The principle of virtual work for the general nonlinear macroscopic model can be directly derived from the principle of virtual work of the full model, by employing the identity (4), which is quite straightforward and therefore the details are omitted here (see Damil and Potier-Ferry, 2008 for more information).

This nonlinear macroscopic model can be easily discretized by classical 3D brick finite elements and an interesting 2D numerical application has been performed to couple global–local buckling modes of sandwich beams (Mhada et al., 2013). Nevertheless, in order to be consistent with the simplest film/substrate models in the literature (Audoly and Boudaoud, 2008a; Chen and Hutchinson, 2004; Huang et al., 2005; Xu et al., 2015b), in what follows, we will limit ourselves to a linear elastic solid in the substrate and a nonlinear Föppl–von Kármán plate model in the film.

3. A 3D macroscopic film/substrate model

The general macroscopic modeling framework presented above can be directly applied to 3D discretization of film/substrate systems. However, considering the intrinsic property of the film thinness that has been previously discussed in Xu (2014) and Xu et al. (2014b, 2015a), direct 3D discretization is cumbersome and especially not efficient for very thin films, since a huge ratio of thickness between the film and the substrate requires extremely refined meshes to keep the acceptable

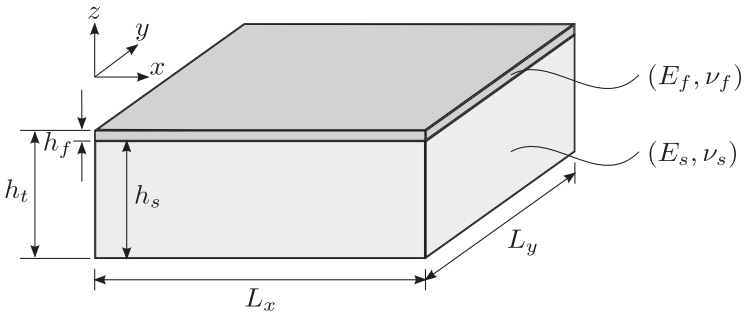

Fig. 2. Geometry of film/substrate system.

element aspect ratio. One efficient modeling way is to take into account some kinematic simplifications for the film or to employ beam/plate/shell elements that are competitive for thin-walled structure modeling (Xu et al., 2014b, 2015b). This idea leads to the energy separation of the film/substrate system into two parts, i.e. the film and the substrate:

$$\mathbf{\Pi} = \mathbf{\Pi}_f + \mathbf{\Pi}_s. \tag{10}$$

Thus, in what follows, we will incorporate the general macroscopic modeling framework with nonlinear Föppl–von Kármán plate theory to derive a macroscopic plate model representing the film and a macroscopic linear elastic solid describing the substrate, and these two models are then coupled by introducing Lagrange multipliers. The corresponding macroscopic plate model has been presented and validated with application to membrane wrinkling in Damil et al. (2013, 2014). The same plate model will be employed and coupled with a macroscopic linear elastic solid model in the substrate.

We consider an elastic thin film bonded to an elastic substrate, which can buckle under compression. Upon wrinkling, the film elastically buckles to relax the compressive stress and the substrate concurrently deforms to maintain perfect bonding at the interface. The film/substrate system is considered to be three-dimensional and the geometry is as shown in Fig. 2. Let x and y be in-plane coordinates, while z is the direction perpendicular to the mean plane of the film/substrate. The width and length of the system are denoted by L_x and L_y, respectively. The parameters h_f, h_s and h_t represent, respectively, the thickness of the film, the substrate and the total thickness of the system. Young's modulus and Poisson's ratio of the film are respectively denoted by E_f and ν_f, while E_s and ν_s are the corresponding material properties for the substrate.

In the following, the elastic potential energy of the system is considered in the framework of Hookean elasticity. The large range of stiffness ratio E_f/E_s, from $O(1)$ to $O(10^5)$, has been previously discussed in Xu et al. (2014b, 2015a,b). It has been discussed that in the case of a large stiffness ratio $E_f/E_s \approx O(10^4) \sim O(10^5)$, critical strains are very small and thus Hookean linear elastic framework is relevant (Xu et al., 2014b, 2015a). In this paper, we limit ourselves to this small strain framework, but it could be flexibly extended to the framework of finite strain hyperelasticity as in Xu et al. (2015a), when considering much softer films with a small stiffness ratio.

3.1. Nonlinear macroscopic plate model for the film

In the literature, most of the authors model the film by Föppl–von Kármán nonlinear elastic plate theory (Audoly and Boudaoud, 2008a; Chen and Hutchinson, 2004; Huang et al., 2005; Xu et al., 2015b), which implies moderate rotations and small strains. When the film wrinkles, the wavelength is much larger than the film thickness, so that Föppl–von Kármán nonlinear elastic plate theory can adequately model the thin film (Landau and Lifshitz, 1959).

The technique of slowly variable Fourier coefficients will be recalled to deduce the macroscopic plate model based on the well-known Föppl–von Kármán equations for elastic isotropic plates:

$$\begin{cases} D_b \Delta^2 w - \operatorname{div}\left(\mathbf{N}_m \cdot \nabla w\right) = 0, \\ \mathbf{N}_m = \mathbf{L}_m \cdot \gamma, \\ \gamma = \dfrac{1}{2}\left(\nabla \mathbf{u} + {}^t\nabla \mathbf{u}\right) + \dfrac{1}{2}\left(\nabla w \otimes \nabla w\right), \\ \operatorname{div} \mathbf{N}_m = 0, \end{cases} \tag{11}$$

where $\mathbf{u} = (u, v) \in \mathbb{R}^2$ represents the in-plane displacement, while w is the deflection. The flexural rigidity of the plate is expressed as $D_b = E_f h_f^3/12(1-\nu_f^2)$. The membrane stress and strain are denoted by $\mathbf{N}_m$ and γ, respectively. With the vectorial notations $\mathbf{N}_m = {}^t\{N_X, N_Y, N_{XY}\}$ and $\gamma = {}^t\{\gamma_X, \gamma_Y, \gamma_{XY}\}$, the membrane elastic matrix can be written as

$$\mathbf{L}_m = \frac{E_f h_f}{1-\nu_f^2}\begin{bmatrix} 1 & \nu_f & 0 \\ \nu_f & 1 & 0 \\ 0 & 0 & \dfrac{1-\nu_f}{2} \end{bmatrix}. \tag{12}$$

The potential energy of the film, $\mathbf{\Pi}_f$, can be divided into a membrane part $\mathbf{\Pi}_{mem}$ and a bending part $\mathbf{\Pi}_{ben}$:

$$\begin{cases} \mathbf{\Pi}_f(\mathbf{u}, w) = \mathbf{\Pi}_{mem}(\mathbf{u}, w) + \mathbf{\Pi}_{ben}(w), \\ \mathbf{\Pi}_{mem}(\mathbf{u}, w) = \dfrac{1}{2}\displaystyle\iint_{\Omega_f} {}^t\gamma \cdot \mathbf{L}_m \cdot \gamma \, \mathrm{d}\Omega = \frac{E_f h_f}{2(1-\nu_f^2)} \iint_{\Omega_f} \left(\gamma_X^2 + \gamma_Y^2 + 2(1-\nu_f)\gamma_{XY}^2 + 2\nu_f \gamma_X \gamma_Y\right) \mathrm{d}\Omega, \\ \mathbf{\Pi}_{ben}(w) = \dfrac{D_b}{2}\displaystyle\iint_{\Omega_f} \left((\triangle w)^2 - 2(1-\nu_f)\left(\frac{\partial^2 w}{\partial X^2}\frac{\partial^2 w}{\partial Y^2} - \left(\frac{\partial^2 w}{\partial X \partial Y}\right)^2 \right) \right) \mathrm{d}\Omega. \end{cases} \tag{13}$$

Details on derivation of the macroscopic plate model are recalled in Appendices B and C. The macroscopic model is deduced from the minimum of total energy that is the sum of membrane energy (48) and bending energy (60), which associates zero order harmonic for membrane quantities and real-valued first order harmonics for the deflection. The unknowns of the macroscopic model are the zero order Fourier coefficient $\mathbf{u}(X, Y)$ of the in-plane displacement ($j=0$ in (1)), i.e. its mean

value on a period, and the first envelope $w(X, Y)$ of the transversal oscillation ($j=1$ in (1)) that is further assumed to be real-valued. Hence, this model is very simplified as compared to the one presented in Section 2, but it has been established in Damil et al. (2013, 2014) that it can accurately describe the coupling between wrinkling and membrane behavior. In this way, the total energy is stationary at equilibrium:

$$\delta\mathbf{\Pi}_{mem} + \delta\mathbf{\Pi}_{ben} = 0. \tag{14}$$

The condition that any virtual displacement is zero at the boundary gives

$$\iint_{\Omega_f} \mathbf{N}_m\colon \delta\varepsilon \, \mathrm{d}\Omega = 0, \tag{15}$$

$$\iint_{\Omega_f} \mathbf{N}_m\colon \delta\gamma^{wr} \, \mathrm{d}\Omega + \delta\mathbf{\Pi}_{ben} = 0. \tag{16}$$

After straightforward calculations, one obtains the partial differential equations of the macroscopic problems:

$$\begin{cases} -6D_bQ^2\dfrac{\partial^2 w}{\partial X^2} - 2D_bQ^2\dfrac{\partial^2 w}{\partial Y^2} + \left(D_bQ^4 + N_XQ^2\right)w - \mathrm{div}\left(\mathbf{N}_m\cdot\nabla w\right) = 0, \\ \mathbf{N}_m = \mathbf{L}_m\colon\left[\varepsilon(\mathbf{u}) + \gamma^{wr}(w)\right], \\ \mathrm{div}\,\mathbf{N}_m = 0. \end{cases} \tag{17}$$

where the macroscopic wrinkling term γ^{wr} is defined in Appendix B. The above model (17) couples nonlinear membrane equations with a bifurcation equation satisfied by the envelope of wrinkling pattern. Discretization procedure of the macroscopic model is detailed in Appendix B.

Since the model (17) is a second order partial differential system, any classical C^0 finite element is acceptable for its discretization. In this paper, 8-node quadratic quadrilateral elements (2D-Q8) with three degrees of freedom (u, v, w) per node are employed. Details on finite element discretization will be omitted here, since it is quite classical and straightforward.

3.2. Macroscopic linear elasticity for the substrate

As discussed in Xu et al. (2014b, 2015a,b), since the displacement, rotation and strain remain relatively small in the substrate in the case of a large stiffness ratio $E_f/E_s \approx O(10^4) \sim O(10^5)$, the linear isotropic elasticity theory is sufficient to represent the substrate, while the potential energy of the substrate should be reformulated in the macroscopic framework. We apply the technique of slowly variable Fourier coefficients in 3D cases. To be consistent with the macroscopic plate model, we also assume that the instability wave number vector $\{q\}$ is known and the wave spreads along the O_x direction. In other words, the vector $\{q\}$ is parallel to the unit vector $\{1, 0, 0\}$, i.e. $\{q\} = q\{1, 0, 0\}$. The unknown field $\mathbf{U}(X, Y, Z) = \{\mathbf{u}(X, Y, Z), \sigma(X, Y, Z), \varepsilon(X, Y, Z)\}$, whose components are displacement, stress and strain, is written in the following form:

$$\mathbf{U}(X, Y, Z) = \sum_{j=-1}^{+1} \mathbf{U}_j(X, Y, Z)e^{jiqX}, \tag{18}$$

where the macroscopic unknown fields $\mathbf{U}_j(X, Y, Z)$ vary slowly on the period $[X, X + \frac{2\pi}{q}]$ of oscillations. As discussed before, it is not necessary to choose an infinite number of Fourier coefficients and thus the unknown fields $\mathbf{U}(X, Y, Z)$ are expressed in terms of two harmonics: the mean field $\mathbf{U}_0(X, Y, Z)$ and the first order harmonics $\mathbf{U}_1(X, Y, Z)e^{iqX}$ and $\overline{\mathbf{U}}_1(X, Y, Z)e^{-iqX}$. Hence, the macroscopic potential energy of the substrate can be expressed as

$$\mathbf{\Pi}_s(\mathbf{u}_s) = \frac{1}{2}\int_{\Omega_s} \sum_{j=-1}^{+1} {}^t\varepsilon_{-j}\colon \mathbf{L}_s\colon \varepsilon_j \, \mathrm{d}\Omega, \tag{19}$$

where $\mathbf{L}_s$ is the elastic matrix of the substrate. It can be seen that the macroscopic potential energy (19) takes the same form as the classical one (Xu et al., 2014b). Note that each unknown of the classical model is replaced by a vector of three times larger size, since it takes into account the zero order harmonic and the first order harmonic represented by a complex vector or by two real vectors. These generalized vectors, i.e. the generalized displacement $\{\mathbf{u}_s\}$, the generalized stress $\{\sigma\}$, the generalized strain $\{\varepsilon\}$ and the generalized displacement gradient $\{\theta\}$, are defined as

$$\begin{cases} \{\mathbf{u}_s\} = \{\{\mathbf{u}_0\}, \{\mathbf{u}_1^R\}, \{\mathbf{u}_1^I\}\}, \\ \{\sigma\} = \{\{\sigma_0\}, \{\sigma_1^R\}, \{\sigma_1^I\}\}, \\ \{\varepsilon\} = \{\{\varepsilon_0\}, 2\{\varepsilon_1^R\}, 2\{\varepsilon_1^I\}\}, \\ \{\theta\} = \{\{\theta_0\}, \{\theta_1^R\}, \{\theta_1^I\}\}. \end{cases} \tag{20}$$

For linear elasticity, one can get a constitutive law for the zero order harmonic (real number) and two constitutive laws for the first order harmonic (complex number), all the equations being uncoupled:

$$\begin{cases} \{\varepsilon_0\} = [\mathbf{L}_s]^{-1}\{\sigma_0\} = [\mathbf{H}]\{\theta_0\}, \\ \{\varepsilon_1\} = [\mathbf{L}_s]^{-1}\{\sigma_1\} = [\mathbf{H}]\{\theta_1\}, \end{cases} \tag{21}$$

where the matrix $[\mathbf{H}]$ is defined in Appendix A. Finally, the macroscopic behavior can be formulated in a general form:

$$\begin{cases} \{\sigma\} = [\mathbf{L}_s^{gen}]\{\varepsilon\}, \\ \{\varepsilon\} = [\mathbf{H}^{gen}]\{\theta\}, \end{cases} \tag{22}$$

where

$$[\mathbf{L}_s^{gen}] = \begin{bmatrix} \mathbf{L}_s & 0 & 0 \\ 0 & \mathbf{L}_s/2 & 0 \\ 0 & 0 & \mathbf{L}_s/2 \end{bmatrix}, \tag{23}$$

$$[\mathbf{H}^{gen}] = \begin{bmatrix} \mathbf{H} & 0 & 0 \\ 0 & 2\mathbf{H} & 0 \\ 0 & 0 & 2\mathbf{H} \end{bmatrix}. \tag{24}$$

Discretization of the 3D macroscopic model (19) takes the same shape functions as the 3D full model (Xu et al., 2014b), where the details are omitted since it is quite straightforward. In this paper, 8-node linear brick elements with reduced integration are applied to discretize the substrate, with totally 72 ($3 \times 3 \times 8$) degrees of freedom per element.

3.3. Coupling between the film and the substrate

As the film is bonded to the substrate, the displacement should be continuous at the interface. However, the macroscopic plate elements for the film and 3D macroscopic brick elements for the substrate cannot be simply joined directly since they belong to dissimilar elements. Therefore, additional incorporating constraint equations have to be employed. Hereby, Lagrange multipliers are applied to couple the corresponding nodal displacements of the same order harmonics in compatible meshes between the film and the substrate (see Fig. 3). Note that using 8-node linear brick element here is only for coupling convenience, 20-node quadratic brick element would be another good candidate, while both of them follow the same coupling strategy. Consequently, the stationary function of film/substrate system is given in a Lagrangian form:

$$\mathcal{L}(\mathbf{u}_f, \mathbf{u}_s, \ell) = \mathbf{\Pi}_f + \mathbf{\Pi}_s + \sum_{node\ i} \ell_i\big[\mathbf{u}_f(i) - \mathbf{u}_s(i)\big], \tag{25}$$

where the displacements of the film and the substrate are respectively denoted as $\mathbf{u}_f$ and $\mathbf{u}_s$, while the Lagrange multipliers are represented by ℓ. At the interface, the displacement continuity is satisfied at the same nodes and connects the middle surface of the film and the top surface of the substrate. From Eq. (25), three equations are obtained according to $\delta\mathbf{u}_f$, $\delta\mathbf{u}_s$ and

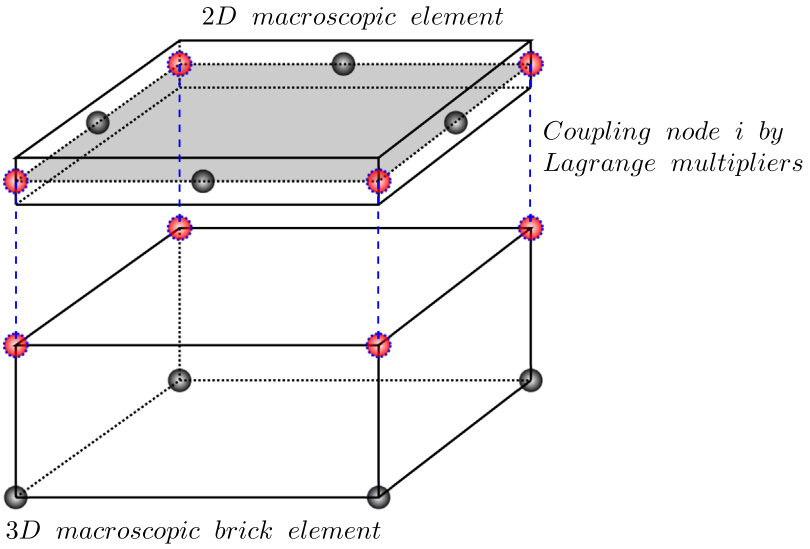

Fig. 3. Sketch of coupling at the interface. The coupling nodes are marked by red color. (For interpretation of the references to color in this figure caption, the reader is referred to the web version of this paper.)

Table 1
Common characteristics of material and geometric properties.

E_f (MPa)	E_s (MPa)	ν_f	ν_s	h_f (mm)	h_s (mm)
1.3×10^5	1.8	0.3	0.48	10^{-3}	0.1

$\delta\ell$:

$$\begin{cases} \delta\boldsymbol{\Pi}_f + \sum\limits_{node\ i} \ell_i \delta\mathbf{u}_f(i) = 0, \\ \delta\boldsymbol{\Pi}_s - \sum\limits_{node\ i} \ell_i \delta\mathbf{u}_s(i) = 0, \\ \sum\limits_{node\ i} \delta\ell_i \mathbf{u}_f(i) - \sum\limits_{node\ i} \delta\ell_i \mathbf{u}_s(i) = 0. \end{cases} \tag{26}$$

4. Path-following technique

The partial differential Eq. (17) is a type of nonlinear Poisson's equation that is coupled with the macroscopic linear elastic model developed in Section 3.2, as illustrated in Eq. (25). Thus, it is not too complicated to discretize this coupled problem and to solve it numerically, for instance by using classical predictor–corrector algorithms such as the Newton–Raphson procedure or path-following techniques such as arc-length type methods. In this paper, Asymptotic Numerical Method (ANM) (Cochelin, 1994; Cochelin et al., 1994, 2007; Damil and Potier-Ferry, 1990) is applied to solve the resulting nonlinear equations. The ANM is a path-following technique that is based on a succession of high order power series expansions (perturbation technique) with respect to a well chosen path parameter, which appears as an efficient continuation predictor without any corrector iteration. Besides, one can get approximations of the solution path that are very accurate inside the radius of convergence. In this paper, the main interest of the ANM is its ability to trace the post-buckling evolution and predict secondary bifurcations without any special tool. Precisely, accumulation of small steps in the ANM is often associated with the occurrence of a bifurcation (Xu, 2014; Xu et al., 2014b, 2015b). The ANM has been successfully applied to both 2D and 3D classical film/substrate models (Xu et al., 2014b, 2015b) and even incorporated with Automatic Differentiation techniques to solve hyperelasticity problems recently (Xu et al., 2015a). This path-following technique is also suitable for the presented macroscopic models and the scheme remains unchanged. More details on implementation of the ANM can be found in Xu (2014) and Xu et al. (2014b, 2015a,b).

The resulting nonlinear problem (26) can be rewritten as

$$\delta\mathcal{L}(\mathbf{u}_f, \mathbf{u}_s, \ell) = \left\langle \mathbf{R}(\mathbf{U}, \lambda), \delta\mathbf{U} \right\rangle = 0, \tag{27}$$

where $\mathbf{U} = (\mathbf{u}_f, \mathbf{u}_s, \ell)$ is a mixed vector of unknowns and $\mathbf{R}$ is the residual vector. The external load parameter is denoted as a scalar λ. The principle of the ANM continuation consists in describing the solution path by computing a succession of truncated power series expansions. From a known solution point $(\mathbf{U}_0, \lambda_0)$, the solution $(\mathbf{U}, \lambda)$ is expanded into truncated power series of a perturbation parameter a:

$$\begin{cases} \mathbf{U}(a) = \mathbf{U}_0 + \sum\limits_{p=1}^{n} a^p \mathbf{U}_p, \\ \lambda(a) = \lambda_0 + \sum\limits_{p=1}^{n} a^p \lambda_p, \end{cases} \tag{28}$$

$$a = \left\langle \mathbf{u} - \mathbf{u}_0, \mathbf{u}_1 \right\rangle + (\lambda - \lambda_0)\lambda_1, \tag{29}$$

Table 2
Different parameters of film/substrate systems.

Case	L_x (mm)	L_y (mm)	Loading
Film/Sub I	1.5	1.5	Uniaxial
Film/Sub II	6	0.75	Uniaxial
Film/Sub III	1.5	1.5	Equi-biaxial
Film/Sub IV	3	3	Equi-biaxial

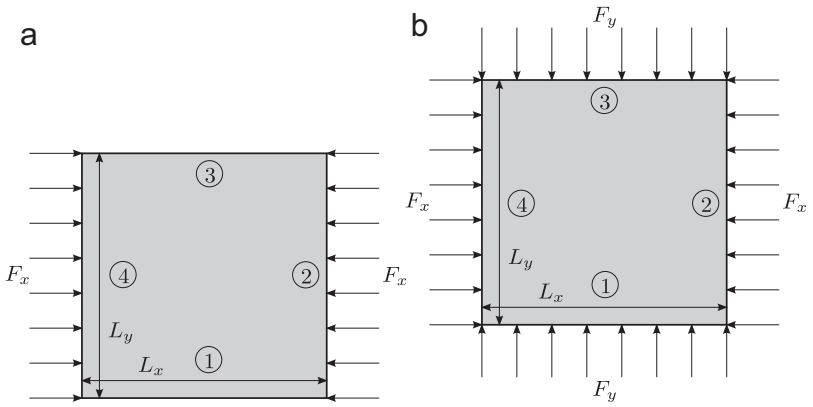

Fig. 4. Loading conditions: (a) Film/Sub I and II under uniaxial compression. (b) Film/Sub III and IV under equi-biaxial compression.

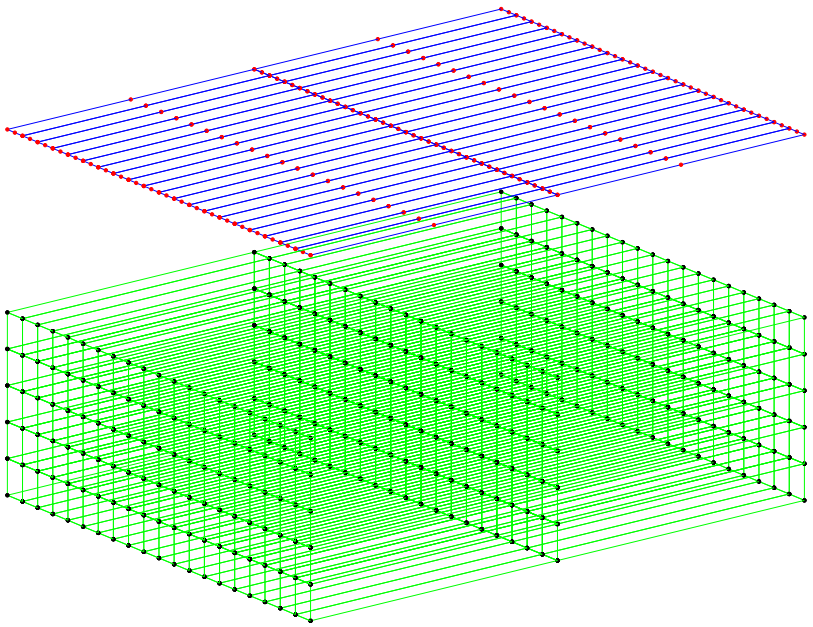

Fig. 5. Initial mesh configuration of Film/Sub I: the film is meshed with 2×20 macroscopic plate elements (blue lines and red nodes) and the substrate is compatibly discretized by $2 \times 20 \times 5$ macroscopic brick elements (green lines and black nodes). (For interpretation of the references to color in this figure caption, the reader is referred to the web version of this paper.)

where n is the truncation order of the series. Eq. (29) defines the path parameter a that can be identified to an arc-length parameter. By introducing Eq. (28) into Eqs. (27) and (29), then equating the terms at the same power of a, one can obtain a set of linear problems. More details of these procedures can be found in Cochelin et al. (1994, 2007) and Xu et al. (2014b, 2015b).

The maximum value of the path parameter a should be automatically defined by analyzing the convergence of the power series at each step. This a_{max} can be based on the difference of displacements at two successive orders that must be smaller than a given precision parameter δ:

$$\text{Validity range:} \quad a_{max} = \left(\delta \frac{\|\mathbf{u}_1\|}{\|\mathbf{u}_n\|} \right)^{1/(n-1)}, \tag{30}$$

where the notation $\|\cdot\|$ stands for the Euclidean norm. Unlike incremental-iterative methods, the arc-length step size a_{max} is adaptive since it is determined *a posteriori* by the algorithm. When there is a bifurcation point on the solution path, the radius of convergence is defined by the distance to the bifurcation. Thus, the step length defined in Eq. (30) becomes smaller and smaller, which looks as if the continuation process 'knocks' against the bifurcation (Baguet and Cochelin, 2003). This accumulation of small steps is a very good indicator of the presence of a singularity on the path. All the bifurcations can be easily identified in this way by the user without any special tool.

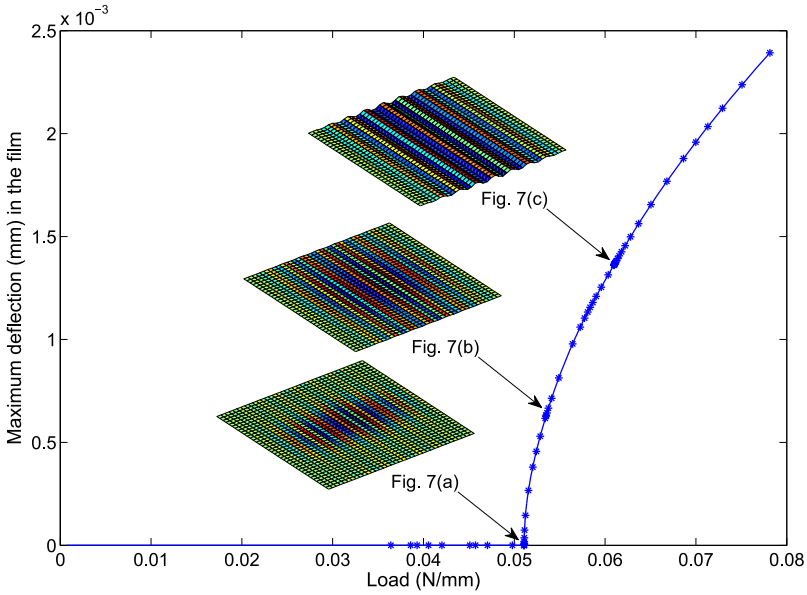

Fig. 6. Bifurcation curve of Film/Sub I under uniaxial compression. Representative wrinkling patterns in Fig. 7 are marked on the post-buckling evolution path. ANM parameters: $n=15$, $\delta = 10^{-8}$, 106 steps. Each point corresponds to one ANM step.

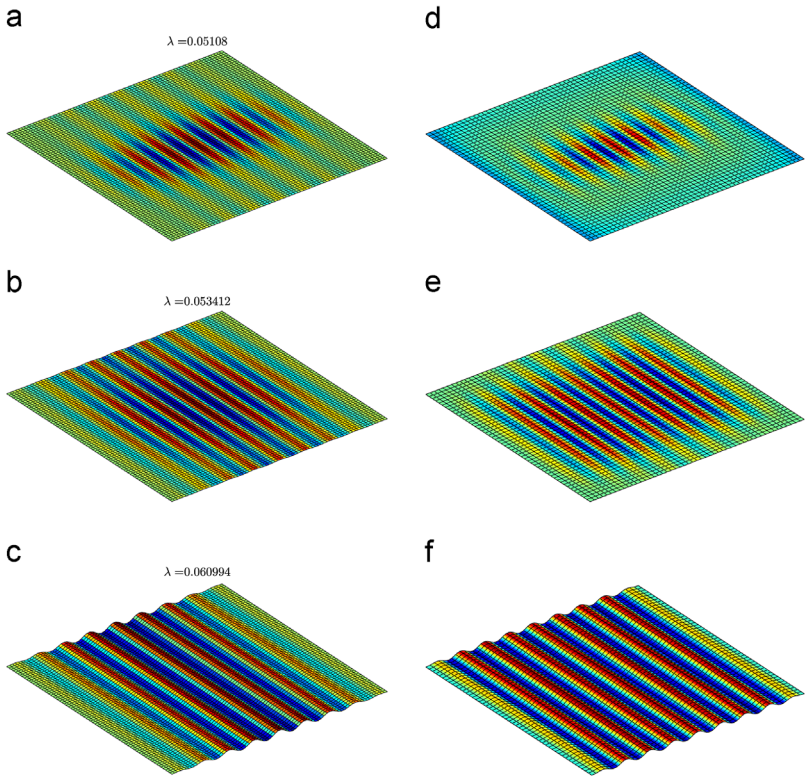

Fig. 7. The left column shows a sequence of representative wrinkling patterns of Film/Sub I under uniaxial compression. The right column presents the results from a full shell/3D model (Xu et al., 2014b): a sequence of representative wrinkling patterns of the film/substrate with clamped boundary conditions under uniaxial compression.

It is worth mentioning that there are only two parameters controlling the algorithm. The first one is the truncation order n of the series. It was previously discussed that the optimal truncation order should be large enough between 10 and 20, but bigger values (*e.g.* $n=50$) lead to good results for large-scale problems as well (Medale and Cochelin, 2009). Another important parameter is the chosen tolerance δ that affects the residual. For instance, very small values of tolerance (*e.g.*

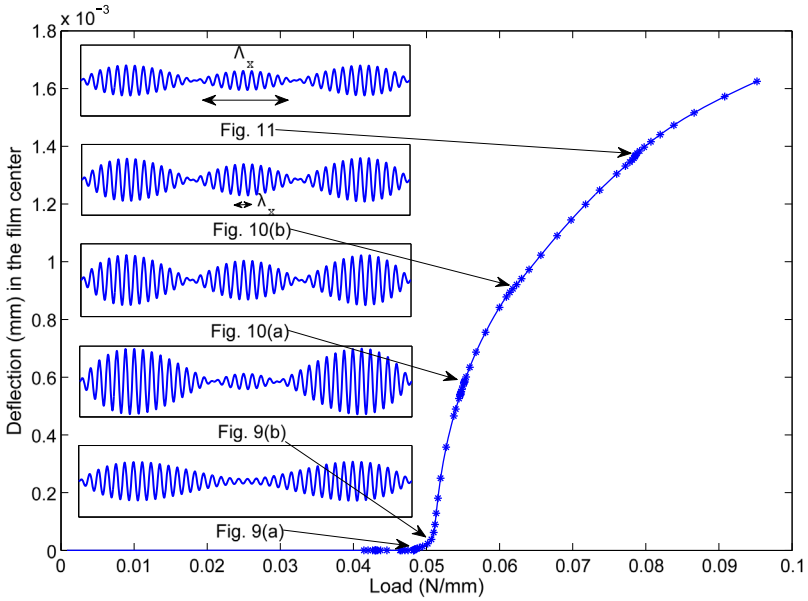

Fig. 8. Bifurcation curve of Film/Sub II under uniaxial compression. Representative wrinkling shapes in Figs. 9, 10 and 11 are marked on the post-buckling evolution path. ANM parameters: $n=15$, $\delta = 10^{-6}$, 135 steps. Each point corresponds to one ANM step.

$\delta = 10^{-6}$) ensure quite a high accuracy and a pretty robust path-following process.

5. Numerical results and discussion

Spatial wrinkling pattern formation and evolution will be investigated based on the established 3D macroscopic film/substrate model, subjected to different loading and boundary conditions. On the bottom surface of the substrate, the zero order and the first order of harmonics u_z are taken to be zero. The material and geometric properties of film/substrate system are the same as those in Xu et al. (2014b, 2015b), which is shown in Table 1. The different dimensional parameters and loading conditions for each case are presented in Table 2 and Fig. 4, respectively. In this paper, the force loading is applied to the film and the substrate is loading free. The huge ratio of Young's modulus, E_f/E_s, determines the critical wavelength λ_c that remains practically unchanged as the amplitude of the wrinkles increases (Huang et al., 2005; Xu et al., 2014b, 2015b). Poisson's ratio is a dimensionless measure of the degree of compressibility. Compliant materials in the substrate, such as elastomers, are nearly incompressible with $\nu_s = 0.48$. In order to trigger a transition from the fundamental branch to the bifurcated one, a small perturbation force, $f_z = 10^{-10}$, is imposed in the center of the film. The introduction of such small perturbation force is quite a common technique in the solution of bifurcation problems by continuation techniques (Allgower and Georg, 1990; Doedel, 1981), even when using commercial finite element codes. This artifice could be avoided by applying a specific procedure to compute the bifurcation branch as in Boutyour et al. (2004) and Vannucci et al. (1998). In this paper, the perturbation force f_z allows one to calculate the whole bifurcated branch with a single continuation algorithm. Bifurcation points are detected by the criterion of small step accumulation. Indeed, when the starting point of the step is close to the bifurcation, the radius of convergence of Taylor series coincides with the distance to the singular point, which explains that the continuation process 'knocks' against the bifurcation (Baguet and Cochelin, 2003). Of course the same step accumulation is observed for a slightly perturbed bifurcation that we shall call 'quasi-bifurcation'. More advanced techniques are available for bifurcation detection such as bifurcation indicator (Xu et al., 2014b, 2015b) and power series analysis in Cochelin and Medale (2013), but the simple detection by sight will prove to be sufficient in our analyses. In what follows, we will explore the formation and evolution of instability patterns through the presented macroscopic model (26).

5.1. Uniaxial compression

First, we investigate the pattern formation and evolution of Film/Sub I that is uniaxially compressed along the x direction as shown in Fig. 4a. The displacements w and u_y are taken to be zero on loading sides ② and ④ (see Fig. 4a) that are parallel to O_y. The other two sides ① and ④ are set to be free. To avoid rigid body motions, the displacement u_x in the film center is locked as well. The film is meshed with 2×20 macroscopic plate elements, where only 2 elements are used along the wave propagation direction (see Fig. 5). The substrate is compatibly discretized by 200 macroscopic brick elements with five layers. Totally, the film/substrate system contains 4086 degrees of freedom (DOF) including the Lagrange multipliers.

The critical load of sinusoidal wrinkles based on classical linearized stability analysis was presented in Chen and

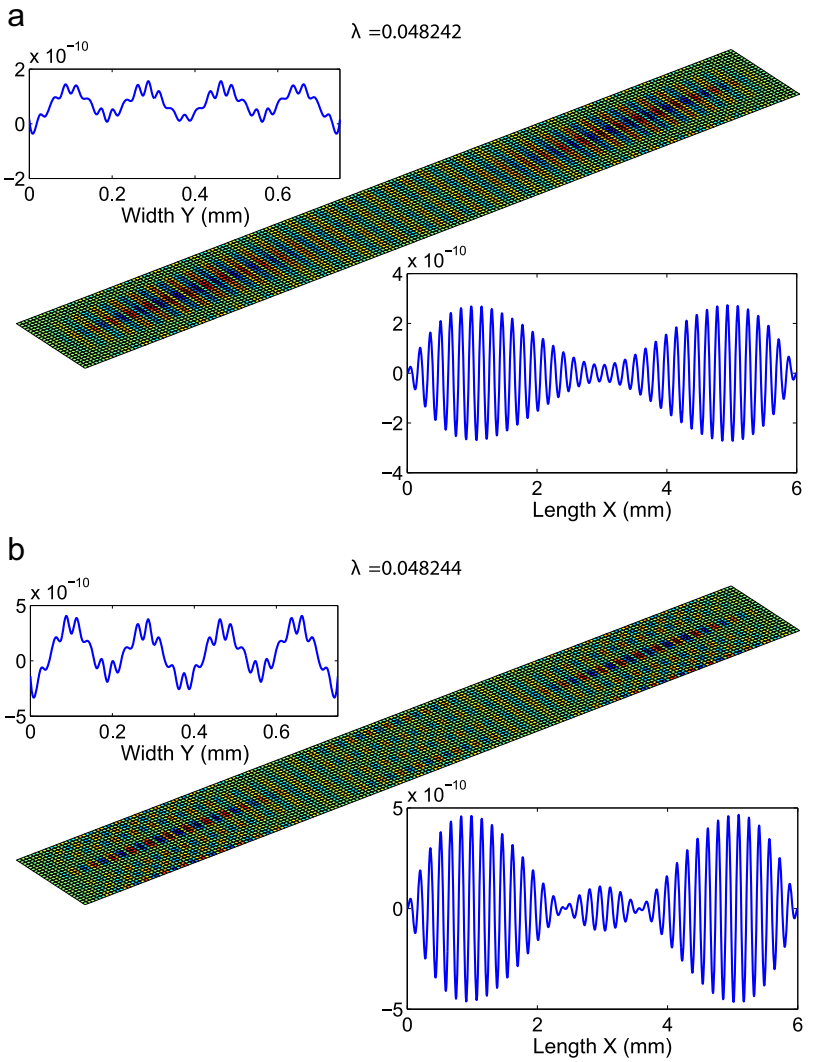

Fig. 9. Representative wrinkling patterns and the associated instability shapes for λ=0.048242 and λ=0.048244 (cross-section at the line $X = 0.5L_x$ and $Y = 0.5L_y$, respectively) of Film/Sub II under uniaxial compression.

Hutchinson (2004) and Huang et al. (2005), with Föppl–von Kármán nonlinear elastic plate assumption for the film. For a thick substrate, the critical load is expressed as $F_c = 1/4h_f\overline{E}_f(3\overline{E}_s/\overline{E}_f)^{2/3}$, where $\overline{E}_f = E_f/(1-\nu_f^2)$ and $\overline{E}_s = E_s/(1-\nu_s^2)$. By introducing the material and geometric parameters in Table 1, one can obtain the analytical solution for periodic boundary conditions F_c = 0.049 N/mm, which is very close to our 3D macroscopic finite element results with real boundary conditions (about 0.051 N/mm in Fig. 6). Besides, as mentioned in Section 2, the wrinkling wave number q is assumed to be chosen *a priori*, which can be either calculated from the linear buckling analysis (Chen and Hutchinson, 2004): $q = 1/h_f(3\overline{E}_s/\overline{E}_f)^{1/3}$, or directly obtained from the classical numerical results in Xu et al. (2014b, 2015b). Consequently, the corresponding critical wavelength can be expressed as $\lambda_c = 2\pi h_f(\overline{E}_f/3\overline{E}_s)^{1/3}$.

The established 3D macroscopic model based on the ANM offers a quite fast computing speed to reach the critical point with a few steps (see Fig. 6). The sequence of wrinkling patterns on the load–displacement curve is illustrated in the left column of Fig. 7. Three bifurcations have been found in the post-buckling range. Instability modes are similar to representative patterns obtained in classical film/substrate models (Xu et al., 2014b, 2015b). Their shapes are sinusoidal with fast oscillations in the compressive direction and with spatial modulation. These oscillations are located in the center of the film at the first bifurcation, which corresponds to the regions where compressive stresses are larger (see Fig. 7a). When the load increases, the sinusoidal shape grows and matures in the bulk (see Fig. 7b and c). From the computational standpoint, the presented macroscopic model can predict the sinusoidal pattern with only 4086 DOF, compared to the previous full model (Xu et al., 2014b) with 41,337 DOF, which dramatically reduces the computational cost by more than 90% in terms of DOF. In terms of computational time, the macroscopic calculation takes only 3 min of CPU time, while the classical model spends more than 3 h of CPU time. This means the computational time is significantly reduced by 98%. However, the

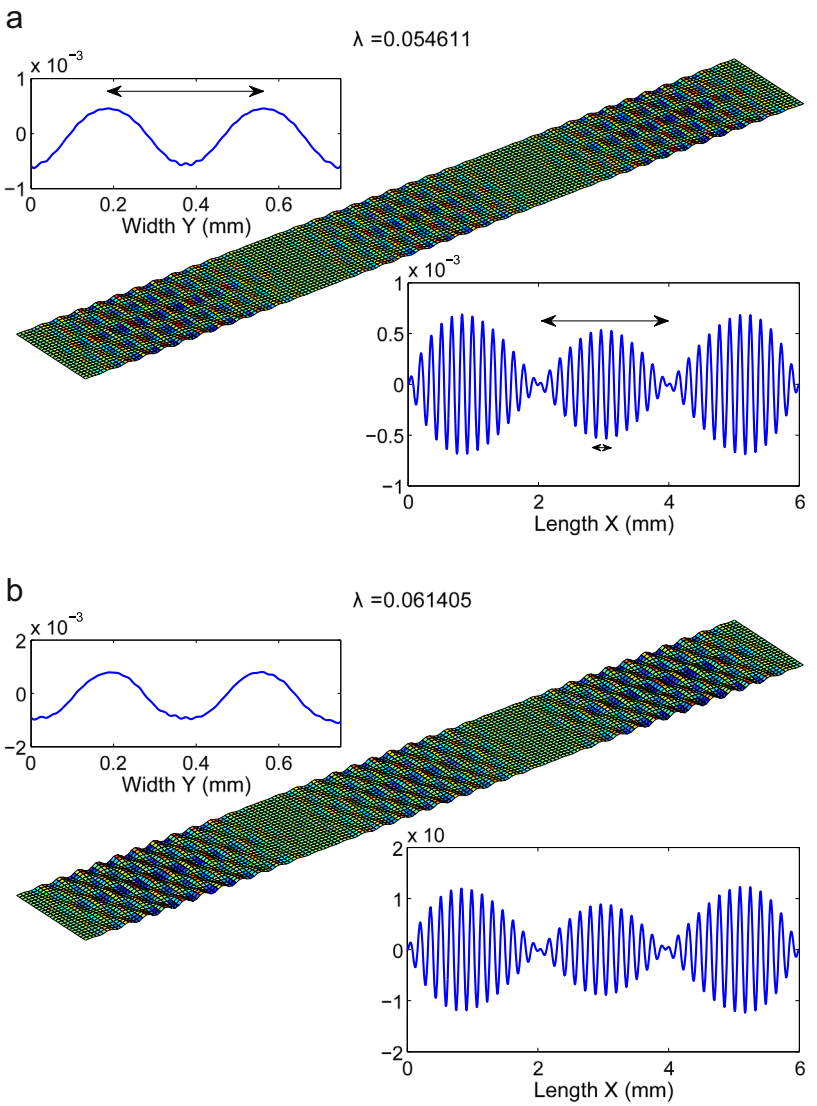

Fig. 10. Representative wrinkling patterns and the associated instability shapes for λ=0.054611 and λ=0.061405 (cross-section at the line $X = 0.5L_x$ and $Y = 0.5L_y$, respectively) of Film/Sub II under uniaxial compression.

intrinsic drawback of any model reduction that a clear and secure account of boundary conditions cannot be obtained (Xu et al., 2014a) would lead to the slight differences of mode shape between the macroscopic model and the classical one (Xu et al., 2014b) (compare the left and the right columns in Fig. 7). Nevertheless, the presented macroscopic reduced model is able to give a reasonably good approximation of these sinusoidal wrinkling patterns.

The important point of the macroscopic reduced-order model lies in its ability to efficiently calculate complicated instability modes with numerous undulations, namely in the case of large wave number. Here, we consider a long rectangular sample with a high aspect ratio, i.e. Film/Sub II with L_x = 6 mm and L_y = 0.75 mm, subjected to uniaxial compression along the x direction as shown in Fig. 4a. Four macroscopic elements are taken along the wave propagation direction x. The other parameters, including material properties, boundary conditions and meshes, remain the same as those in the previous case. The load–displacement curve and the corresponding representative wrinkling patterns are presented in Figs. 8–11. In the initial buckling stage, rapid sinusoidal oscillations appear around the boundary regions. At this level there are two packets of modes with a slowly varying envelope of sinusoidal shape. Then a new packet of undulations emerges and grows in the center gradually. Finally, it ends up with three packets with the same amplitude and macroscopic wavelength Λ_x (see Fig. 10). This is a bit surprising because the most common scenario corresponds to a single packet: it begins with a sinusoidal envelope evolving rapidly to a hyperbolic tangent shape. This usual scenario can be explained from the one-dimensional Ginzburg–Landau equation where the solution is a hyperbolic tangent (Newell and Whitehead, 1969). The classical sine-

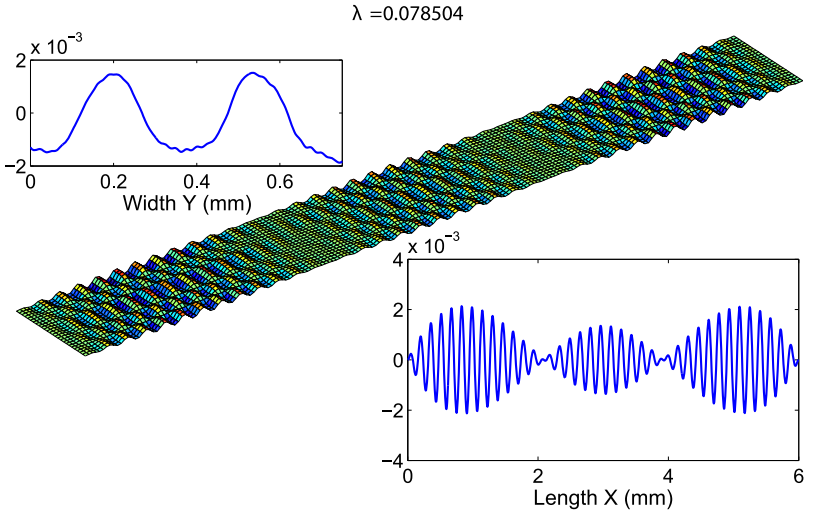

Fig. 11. Representative wrinkling pattern and the associated instability shape for $\lambda = 0.078504$ (cross-section at the line $X = 0.5L_x$ and $Y = 0.5L_y$, respectively) of Film/Sub II under uniaxial compression.

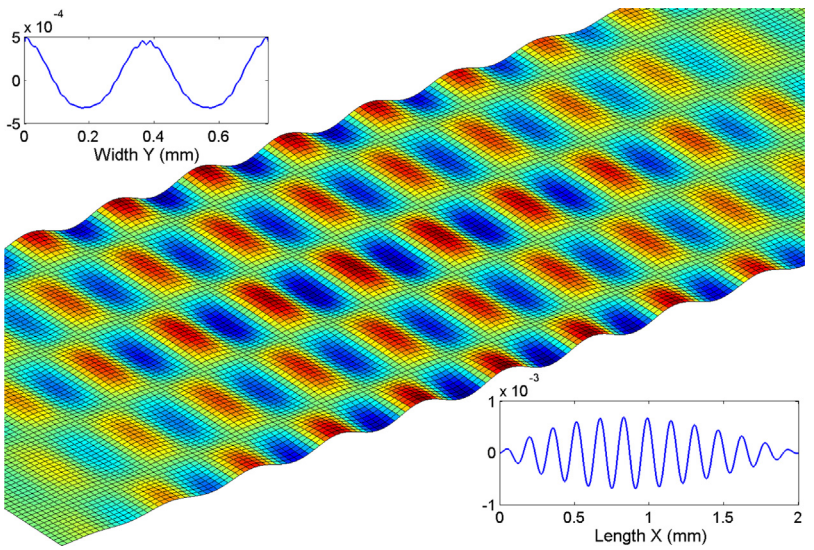

Fig. 12. Zoom of the left boundary region in Fig. 10a.

hyperbolic tangent scheme can be illustrated for instance by numerical results on compressed rectangular membrane (Damil et al., 2014). To check the generality of the three-packet scheme, two other tests have been performed with a shorter ($L_x = 3$ mm) and with a longer length ($L_x = 9$ mm), respectively. As plotted in Fig. 13, the number of packets is always three in the post-buckling range ($\Lambda_x = L_x/3$) and the microscopic wavelength λ_x remains unchanged. As a consequence, the number of oscillations in a packet increases while the total length L_x increases. A similar mode shape has been also observed experimentally in the wrinkling of a stiff silica-like film formed by surface oxidation of a pre-stretched Polydimethylsiloxane (PDMS) substrate, see Fig. 3 in Zang et al. (2012). Hence, we have found numerically a new bifurcation scenario involving several packets of instability waves, which was revealed experimentally as well. For the moment, a theoretical explanation is still lacking.

Besides, newly formed waves spreading along the width direction y, with approximately twice the wavelength ($\lambda_y \approx 2\lambda_x$), have been found in the post-buckling regime (see Figs. 10a and 12). This happens after the first bifurcation along with the development of macroscopic compressive stress N_Y when the load reaches about 0.0535 N/mm (see Fig. 14). Indeed, the transversal stress N_Y is initially tensile, but it becomes compressive after the first bifurcation at the level of 0.0535 N/mm. A number of numerical tests on various ratios of L_x/L_y or L_y/λ_y, *e.g.* $L_x/L_y = 2, 4, 8, 16$, etc. or $L_y/\lambda_y = 1, 2, 4, 8$, etc. have been carried out to explore whether this wavelength is related to the width of the sample. It turns out that the width L_y has no

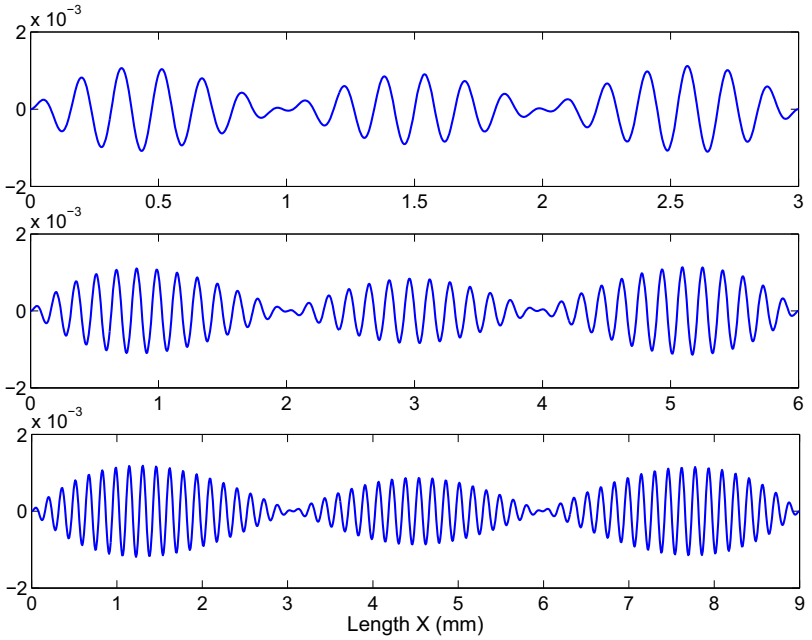

Fig. 13. Wrinkling shapes for $\lambda = 0.06$ with different lengths L_x (cross-section at the line $Y = 0.5L_y$). Three packets of wrinkles are observed with macroscopic wavelength $\Lambda_x = L_x/3$.

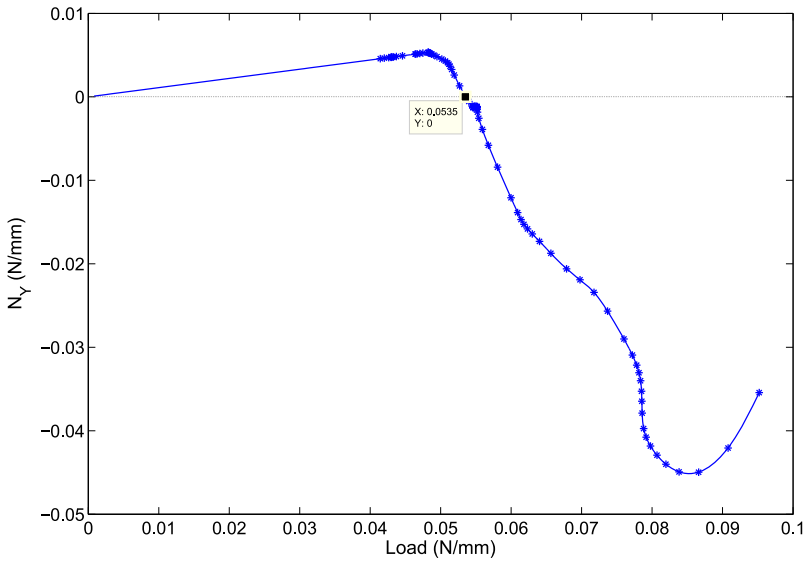

Fig. 14. Film/Sub II under uniaxial compression: macroscopic stress N_Y *vs.* external loading.

apparent effect on the transverse wavelength λ_y. It appears that λ_y depends on material properties and film thickness: it is always in the range $\lambda_y \approx 2\lambda_x \sim 3\lambda_x$.

5.2. *Equi-biaxial compression*

Checkerboard patterns are then explored via Film/Sub III under equi-biaxial compression in both x and y directions (see Fig. 4b). The deflection envelope w on four edges ①, ②, ③ and ④, is locked to be zero, which means the film is clamped on the whole boundary. The displacements u_x and u_y in the film center are set to be zero to avoid rigid body motions. The film is meshed with 2×50 macroscopic elements, where only 2 elements are used along the x direction. The substrate is compatibly discretized by 500 macroscopic brick elements with five layers. In total, the film/substrate system contains 9936 DOF

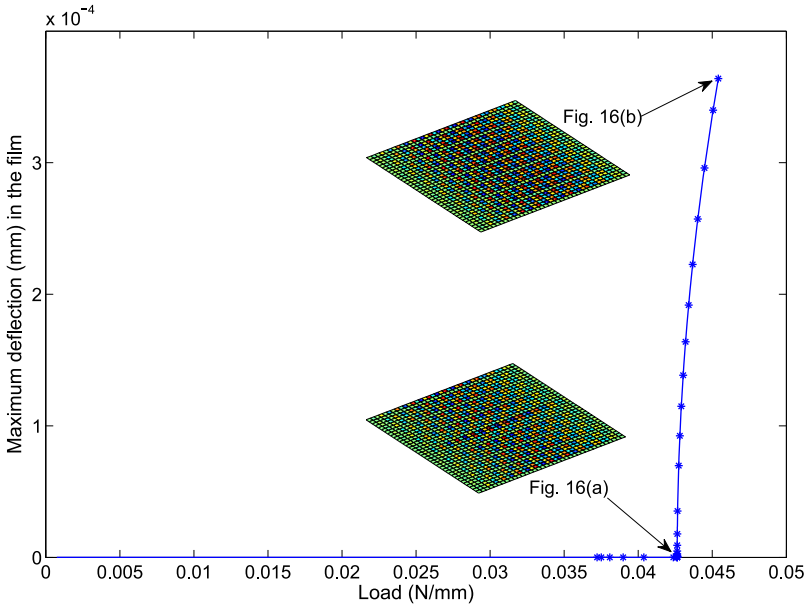

Fig. 15. Bifurcation curve of Film/Sub III under biaxial compression. Representative wrinkling patterns in Fig. 16 are marked on the post-buckling evolution path. ANM parameters: $n=15$, $\delta = 10^{-9}$, 68 steps. Each point corresponds to one ANM step.

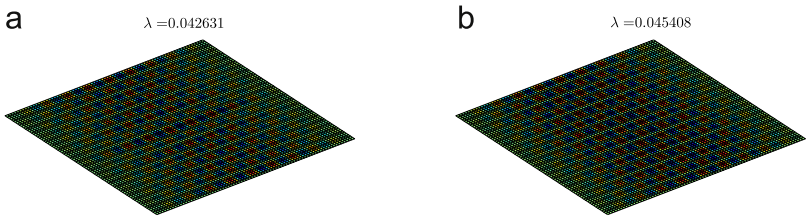

Fig. 16. A sequence of representative wrinkling patterns of Film/Sub III under biaxial compression.

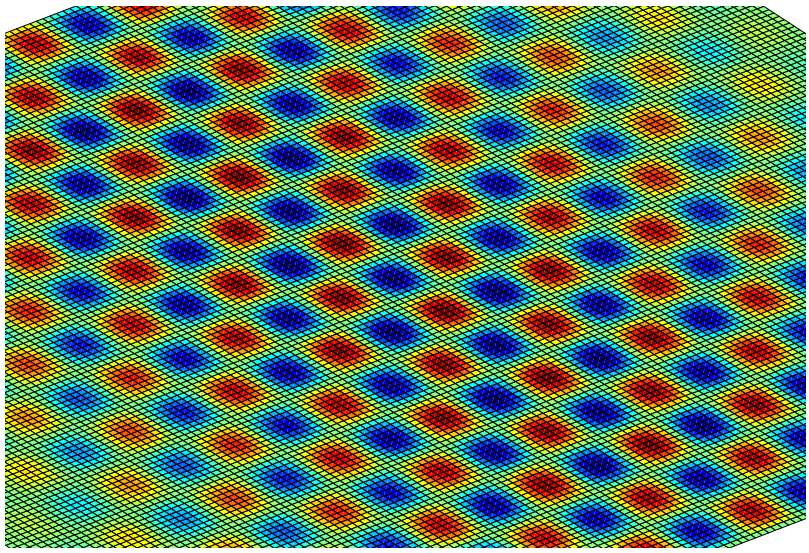

Fig. 17. Zoom of the bulk in Fig. 16b. Square checkerboard patterns appear in the bulk.

including the Lagrange multipliers.

Square checkerboard mode emerges at the bifurcation and then matures in the final step (see Figs. 15 and 16). Compared to the full model in Xu et al. (2014b), the presented macroscopic model is able to predict more uniformly distributed square cells (since the wave number is chosen *a priori*) in the large-scale case of a relatively big wave number (see Fig. 17), with

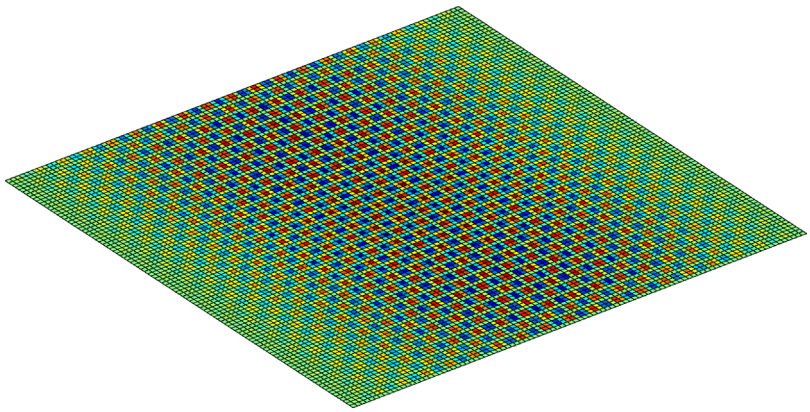

Fig. 18. Square checkerboard patterns with huge wave number obtained via Film/Sub IV.

much fewer elements as mentioned above. The growth of checkerboard patterns appears not to be as stable as sinusoidal patterns, since the maximum loading reaches a rather small value of the deflection ($w/h_f \approx 0.37$) (see Fig. 15). The continuation technique suffers an accumulation of small steps and cannot go farther. This physical phenomenon has been revealed in small-scale cases by full models (Xu et al., 2014b, 2015a) as well. It is worth mentioning that the checkerboard mode is rarely observed in experiments since it is very sensitive to perturbation or imperfection and it mainly occurs under strictly symmetric loading, boundary and geometric conditions.

A bigger sample of Film/Sub IV is taken into account to simulate square checkerboard shape with large wave number (see Fig. 18), by using only 2×100 macroscopic elements for the film and 19686 DOF for the whole structure, while it would be rather difficult to achieve using full models (Xu et al., 2014b, 2015a) due to the huge computational cost. For the first time, it provides a very efficient way to calculate large-scale periodicity of many oscillations with double wavy directions. Nevertheless, the intrinsic drawback of any model reduction that real boundary conditions cannot be introduced leads to the boundary effects (non-uniformly distributed checkerboard patterns) on both left and right sides (see Figs. 16 and 18). A straight way could be to apply bridging techniques (Xu et al., 2014a) to bypass the question of boundary conditions: the macroscopic model is implemented in the bulk while the full model is employed near the boundary and these two models are coupled with Arlequin method (Ben Dhia, 1998; Ben Dhia and Rateau, 2005). In this way, strengths of each model could be fully exploited while their shortcomings are accordingly overcome.

6. Conclusion

Pattern formation and evolution of stiff thin films bonded to soft substrates were investigated from a multi-scale standpoint, which had not been pursued previously. A general macroscopic modeling framework was first developed based on the technique of slowly varying Fourier coefficients, which can be applied to any 3D discretization of a film/substrate system. A simplified 3D macroscopic model was deduced by associating a geometrically nonlinear macroscopic plate model for the film and a macroscopic linear elastic solid for the substrate. The model is able to predict the occurrence and evolution of sinusoidal and square checkerboard patterns with only a few elements along the wave propagation direction, which significantly reduces the computational cost compared to the full model (Xu et al., 2014b) (decreases DOF and CPU time by more than 90% and 98%, respectively). Additionally, the macroscopic reduced-order model can efficiently simulate large-scale complex instability problems with numerous oscillations, i.e. large wave number, which would be quite difficult to achieve using full models due to the high computational cost.

A new bifurcation scenario with alternating packets of large and small undulations has been found numerically in the post-buckling range by the proposed macroscopic model. The numerical results are quite similar to the experimental observations in Zang et al. (2012). The macroscopic wavelength of envelopes seems to be dimension-dependent with $\Lambda_x = L_x/3$, while the wavelength along the width direction appears to be dimension-independent and always satisfies the relation $\lambda_y \approx 2\lambda_x \sim 3\lambda_x$. This post-bifurcation pattern with three packets of modes seems to be robust, while a single packet is predicted by the classical Ginzburg–Landau equation. As for the square checkerboard mode, it appears not to be as stable as sinusoidal patterns. The maximum loading usually arrives at the deflection value of $w/h_f \approx 0.37$, in both full models (Xu et al., 2014b, 2015a) and the presented macroscopic model, at both small and large scales. This phenomenon may merit further investigation.

Acknowledgements

The authors acknowledge the financial support from French National Research Agency ANR (LabEx DAMAS, Grant no. ANR-11-LABX-0008-01).

Appendix A. Matrix definition

According to Cochelin et al. (2007), for classical Saint–Venant Kirchhoff model, the isotropic elastic matrix $[D]$, the linear matrix $[H]$, the quadratic matrix $[A(\theta)]$ and the displacement gradient vector $\{\theta\}$ can be respectively expressed as

$$[D] = \frac{E}{(1+\nu)(1-2\nu)} \begin{bmatrix} 1-\nu & \nu & \nu & 0 & 0 & 0 \\ \nu & 1-\nu & \nu & 0 & 0 & 0 \\ \nu & \nu & 1-\nu & 0 & 0 & 0 \\ 0 & 0 & 0 & (1-2\nu)/2 & 0 & 0 \\ 0 & 0 & 0 & 0 & (1-2\nu)/2 & 0 \\ 0 & 0 & 0 & 0 & 0 & (1-2\nu)/2 \end{bmatrix}, \tag{31}$$

$$[H] = \begin{bmatrix} 1 & 0 & 0 & 0 & 0 & 0 & 0 & 0 & 0 \\ 0 & 0 & 0 & 0 & 1 & 0 & 0 & 0 & 0 \\ 0 & 0 & 0 & 0 & 0 & 0 & 0 & 0 & 1 \\ 0 & 1 & 0 & 1 & 0 & 0 & 0 & 0 & 0 \\ 0 & 0 & 1 & 0 & 0 & 0 & 1 & 0 & 0 \\ 0 & 0 & 0 & 0 & 0 & 1 & 0 & 1 & 0 \end{bmatrix}, \tag{32}$$

$$[A(\theta)] = \begin{bmatrix} \theta_1 & 0 & 0 & \theta_4 & 0 & 0 & \theta_7 & 0 & 0 \\ 0 & \theta_2 & 0 & 0 & \theta_5 & 0 & 0 & \theta_8 & 0 \\ 0 & 0 & \theta_3 & 0 & 0 & \theta_6 & 0 & 0 & \theta_9 \\ \theta_2 & \theta_1 & 0 & \theta_5 & \theta_4 & 0 & \theta_8 & \theta_7 & 0 \\ \theta_3 & 0 & \theta_1 & \theta_6 & 0 & \theta_4 & \theta_9 & 0 & \theta_7 \\ 0 & \theta_3 & \theta_2 & 0 & \theta_6 & \theta_5 & 0 & \theta_9 & \theta_8 \end{bmatrix}, \tag{33}$$

$$\{\theta\} = \{\nabla \mathbf{u}\} = {}^t\left\{\frac{\partial u}{\partial x}, \frac{\partial u}{\partial y}, \frac{\partial u}{\partial z}, \frac{\partial v}{\partial x}, \frac{\partial v}{\partial y}, \frac{\partial v}{\partial z}, \frac{\partial w}{\partial x}, \frac{\partial w}{\partial y}, \frac{\partial w}{\partial z}\right\} = {}^t\{\theta_1, \theta_2, \theta_3, \theta_4, \theta_5, \theta_6, \theta_7, \theta_8, \theta_9\}, \tag{34}$$

where E and ν represent Young's modulus and Poisson's ratio, respectively.

In the general nonlinear macroscopic model (8), the matrices that represent linear relationships are block-diagonal since the couplings between harmonics appear only for nonlinear terms, which leads to

$$\left[D^{gen}\right] = \begin{bmatrix} D & 0 & 0 & 0 & 0 \\ 0 & D/2 & 0 & 0 & 0 \\ 0 & 0 & D/2 & 0 & 0 \\ 0 & 0 & 0 & D/2 & 0 \\ 0 & 0 & 0 & 0 & D/2 \end{bmatrix}, \tag{35}$$

$$\left[H^{gen}\right] = \begin{bmatrix} H & 0 & 0 & 0 & 0 \\ 0 & 2H & 0 & 0 & 0 \\ 0 & 0 & 2H & 0 & 0 \\ 0 & 0 & 0 & 2H & 0 \\ 0 & 0 & 0 & 0 & 2H \end{bmatrix}. \tag{36}$$

The nonlinear aspects are taken into account by a single matrix:

$$\left[A^{gen}(\Theta)\right] = 2\begin{bmatrix} A(\theta_0)/2 & A(\theta_1^R) & A(\theta_1^I) & A(\theta_2^R) & A(\theta_2^I) \\ 0 & A(\theta_0) & 0 & A(\theta_1^R) & A(\theta_1^I) \\ 0 & 0 & A(\theta_0) & -A(\theta_1^I) & A(\theta_1^R) \\ 0 & A(\theta_1^R)/2 & -A(\theta_1^I)/2 & A(\theta_0) & 0 \\ 0 & A(\theta_1^I)/2 & A(\theta_1^R)/2 & 0 & A(\theta_0) \end{bmatrix}. \tag{37}$$

The size of this matrix is 30×45 in 3D cases and 15×20 in 2D cases.

Note that the jth component of the displacement gradient is not the gradient of the jth component of the displacement (Damil and Potier-Ferry, 2008). The rule defining the Fourier components of a gradient vector reads

$$\{\nabla \mathbf{u}\}_j = \{\nabla(u_j)\} + ji[\mathbf{Q}]\{u_j\}, \tag{38}$$

where

$$\left[\mathbf{Q}\right] = \begin{bmatrix} \{q\} & 0 & 0 \\ 0 & \{q\} & 0 \\ 0 & 0 & \{q\} \end{bmatrix}. \tag{39}$$

Appendix B. Macroscopic modeling of membrane energy

We adapt the technique of Fourier series with slowly variable coefficients in 2D cases (Damil et al., 2014). For simplicity, we suppose that the instability wave number Q is known and the considered wrinkles spread only in the O_x direction. The unknown field $\mathbf{U}(X, Y) = \{\mathbf{u}(X, Y), w(X, Y), \mathbf{N}_m(X, Y), \gamma(X, Y)\}$, whose components are in-plane displacement, transverse displacement, membrane stress and strain, is written in the following form:

$$\mathbf{U}(X, Y) = \sum_{j=-\infty}^{+\infty} \mathbf{U}_j(X, Y) e^{jiQX}, \tag{40}$$

where the macroscopic unknown fields $\mathbf{U}_j(X, Y)$ vary slowly on the period $[X, X + \frac{2\pi}{Q}]$ of oscillations. It is not necessary to choose an infinite number of Fourier coefficients, so the unknown fields $\mathbf{U}(X, Y)$ are expressed in terms of two harmonics: the mean field $\mathbf{U}_0(X, Y)$ and the first order harmonics $\mathbf{U}_1(X, Y)e^{iQX}$ and $\overline{\mathbf{U}}_1(X, Y)e^{-iQX}$. The second harmonic should be taken into account to recover the results of the asymptotic Ginzburg–Landau double-scale approach (Damil and Potier-Ferry, 2010). Nevertheless, the second harmonic does not contribute to the membrane energy in the present case, since the rapid one-dimensional oscillations e^{iQX} are not extensional so that $\mathbf{N}_{m2} = 0$, $w_2 = 0$. Hence the second harmonic does not influence the simplest macroscopic models. A unique direction O_x for wave propagation is chosen in the whole domain. This assumption is a bit restrictive so that the current model can only describe sinusoidal pattern, which should be improved in the future. In principle, the mean field $\mathbf{U}_0(X, Y)$ is real and the envelope $\mathbf{U}_1(X, Y)$ is complex-valued. However, spatial evolutions of patterns can be reasonably accounted for with only two real coefficients in practice, even though a complex envelope can improve the treatment of boundary conditions (Mhada et al., 2012).

After extending derivation rules in two-dimensional framework, the first Fourier coefficient of the gradient and the zero order coefficient of strain (i.e. mean value on a period) can be respectively expressed as

$$\{(\nabla w)_1\} = \begin{Bmatrix} \dfrac{\partial w_1}{\partial X} + iQw_1 \\ \dfrac{\partial w_1}{\partial Y} \end{Bmatrix}, \tag{41}$$

$$\{\gamma_0\} = \begin{Bmatrix} \gamma_{X0} \\ \gamma_{Y0} \\ 2\gamma_{XY0} \end{Bmatrix} = \{\gamma^{FK}\} + \{\gamma^{wr}\}, \tag{42}$$

in which

$$\{\gamma^{FK}\} = \begin{Bmatrix} \dfrac{\partial u_0}{\partial X} + \dfrac{1}{2}\left(\dfrac{\partial w_0}{\partial X}\right)^2 \\ \dfrac{\partial v_0}{\partial Y} + \dfrac{1}{2}\left(\dfrac{\partial w_0}{\partial Y}\right)^2 \\ \dfrac{\partial u_0}{\partial Y} + \dfrac{\partial v_0}{\partial X} + \dfrac{\partial w_0}{\partial X}\dfrac{\partial w_0}{\partial Y} \end{Bmatrix}, \tag{43}$$

$$\{\gamma^{wr}\} = \begin{Bmatrix} \left|\dfrac{\partial w_1}{\partial X} + iQw_1\right|^2 \\ \left|\dfrac{\partial w_1}{\partial Y}\right|^2 \\ \left(\dfrac{\partial w_1}{\partial X} + iQw_1\right)\dfrac{\partial \overline{w}_1}{\partial Y} + \left(\dfrac{\partial \overline{w}_1}{\partial X} - iQ\overline{w}_1\right)\dfrac{\partial w_1}{\partial Y} \end{Bmatrix}, \tag{44}$$

where the strain is divided into a classical part γ^{FK} that takes the same form as the initial Föppl–von Kármán model (11), and a wrinkling part γ^{wr} that depends only on the envelope of deflection w_1.

The strain–displacement law (42) can be simplified. First, the displacement field is reduced to a membrane mean displacement and to a bending wrinkling, i.e. $\mathbf{u}_1 = 0$, $w_0 = 0$, which only considers the influence of wrinkling on a flat membrane state. Second, the deflection envelope $w_1(X, Y)$ is assumed to be real, which disregards the phase modulation of the wrinkling pattern. Therefore, the envelope of the displacement has only three components $\mathbf{u}_0 = (u_0, v_0)$ and w_1 that will be rewritten for simplicity as $(u, v, w) = (u_0, v_0, w_1)$. Consequently, the simplified version of the strain field becomes

$$\{\gamma\} = \{\gamma_0\} = \{\varepsilon(\mathbf{u})\} + \{\gamma^{wr}\}, \tag{45}$$

in which

$$\{\varepsilon(\mathbf{u})\} = \begin{Bmatrix} \dfrac{\partial u}{\partial X} \\ \dfrac{\partial v}{\partial Y} \\ \dfrac{\partial u}{\partial Y} + \dfrac{\partial v}{\partial X} \end{Bmatrix}, \tag{46}$$

$$\{\gamma^{wr}\} = \begin{Bmatrix} \left(\dfrac{\partial w}{\partial X}\right)^2 + Q^2w^2 \\ \left(\dfrac{\partial w}{\partial Y}\right)^2 \\ 2\dfrac{\partial w}{\partial X}\dfrac{\partial w}{\partial Y} \end{Bmatrix}. \tag{47}$$

The simplified membrane strain (45) is quite similar to that of the initial Föppl–von Kármán model. It is split, first in a linear part $\varepsilon(\mathbf{u})$ that is the symmetric part of the mean displacement gradient corresponding to the pure membrane linear strain, second in a nonlinear part γ^{wr} more or less equivalent to wrinkling strain. The main difference with the initial Föppl–von Kármán strain (11) is the extension Q^2w^2 in the wave direction of wrinkles. This wrinkling strain is a stretching and is always positive. In the case of a compressive membrane strain, this wrinkling term leads to a decrease of the true strain. By only considering the zero order harmonic, the reduced membrane energy becomes

$$\begin{aligned} &\mathbf{\Pi}_{mem}(\mathbf{u}, w) \\ &= \frac{E_f h_f}{2(1-\nu_f^2)} \iint_{\Omega_f} \left\{ \left(\frac{\partial u}{\partial X} + \left(\frac{\partial w}{\partial X}\right)^2 + Q^2w^2 \right)^2 + \left(\frac{\partial v}{\partial Y} + \left(\frac{\partial w}{\partial Y}\right)^2 \right)^2 + 2(1-\nu_f)\left(\frac{1}{2}\left(\frac{\partial u}{\partial X} + \frac{\partial v}{\partial Y} \right) + \frac{\partial w}{\partial X}\frac{\partial w}{\partial Y} \right)^2 \right. \\ &\left. + 2\nu_f \left(\frac{\partial u}{\partial X} + \left(\frac{\partial w}{\partial X}\right)^2 + Q^2w^2 \right)\left(\frac{\partial v}{\partial Y} + \left(\frac{\partial w}{\partial Y}\right)^2 \right) \right\} \mathrm{d}\Omega. \end{aligned} \tag{48}$$

The membrane energy (48) is a quadratic function of the membrane strain γ given in (45) that is a quadratic function of displacement. The displacement field and its derivatives can be expressed in the vector form:

$$\{\theta\} = {}^t\left\langle \frac{\partial u}{\partial X}, \frac{\partial u}{\partial Y}, \frac{\partial v}{\partial X}, \frac{\partial v}{\partial Y}, w, \frac{\partial w}{\partial X}, \frac{\partial w}{\partial Y} \right\rangle. \tag{49}$$

The strain is then represented by a constant matrix $[\mathbf{H}_m]$ and a matrix $[\mathbf{A}_m(\theta)]$ that linearly depends on the displacement:

$$\{\gamma\} = \left([\mathbf{H}_m] + \frac{1}{2}[\mathbf{A}_m(\theta)] \right)\{\theta\}, \tag{50}$$

where

$$[\mathbf{H}_m] = \begin{bmatrix} 1 & 0 & 0 & 0 & 0 & 0 & 0 \\ 0 & 0 & 0 & 1 & 0 & 0 & 0 \\ 0 & 1 & 1 & 0 & 0 & 0 & 0 \end{bmatrix}, \tag{51}$$

$$[\mathbf{A}_m(\theta)] = 2\begin{bmatrix} 0 & 0 & 0 & 0 & Q^2 w & \dfrac{\partial w}{\partial X} & 0 \\ 0 & 0 & 0 & 0 & 0 & 0 & \dfrac{\partial w}{\partial Y} \\ 0 & 0 & 0 & 0 & 0 & \dfrac{\partial w}{\partial Y} & \dfrac{\partial w}{\partial X} \end{bmatrix}. \tag{52}$$

With these notations, the variational form of the membrane energy reads

$$\delta\mathbf{\Pi}_{mem}(\mathbf{u}, w) = \iint_{\Omega_f} \langle \delta\theta \rangle \left({}^t[\mathbf{H}_m] + {}^t [\mathbf{A}_m(\theta)] \right)\{\mathbf{N}_m\} \, \mathrm{d}\Omega, \tag{53}$$

where the membrane constitutive law reads

$$\{\mathbf{N}_m\} = \left[\mathbf{L}_m \right] \left([\mathbf{H}_m] + \frac{1}{2}[\mathbf{A}_m(\theta)] \right)\{\theta\}. \tag{54}$$

Appendix C. Macroscopic modeling of bending energy

Through simplifying the energy by keeping only the zero order term, it provides a formulation easier to be managed for the numerical discretization. The computation of the energy is based on the fact that only the zero order harmonic φ_0 of a function φ has a non-zero mean value:

$$\iint_{\Omega_f} \varphi \, \mathrm{d}\Omega = \iint_{\Omega_f} \varphi_0 \, \mathrm{d}\Omega. \tag{55}$$

This identity is applied to the bending energy in the framework $\mathbf{u}_1 = (u_1, v_1) = (0, 0)$, $w_0 = 0$, $w_1 \in \mathbb{R}$:

$$\varphi = \left(\Delta w\right)^2 - 2(1 - \nu_f)\left(\frac{\partial^2 w}{\partial X^2}\frac{\partial^2 w}{\partial Y^2} - \left(\frac{\partial^2 w}{\partial X \partial Y} \right)^2 \right) = \varphi^A - 2(1 - \nu_f)\varphi^B. \tag{56}$$

The first terms of bending energy reads

$$\varphi_0^A = \left(\Delta w\right)^2 = \sum_{j=-\infty}^{+\infty} \left(\Delta w\right)_j \left(\Delta w\right)_{-j} = 2\left(\Delta w\right)_1 \left(\Delta w\right)_{-1} = 2\left| \left(\Delta w\right)_1 \right|^2 = 2\left| \Delta w_1 - Q^2 w_1 + 2iQ\frac{\partial w_1}{\partial X} \right|^2. \tag{57}$$

Due to the assumption of a real envelope $w = w_1$, the first term of the bending energy can be expressed as

$$\varphi_0^A = 2\left(\Delta w - Q^2 w\right)^2 + 8Q^2\left(\frac{\partial w}{\partial X} \right)^2. \tag{58}$$

In the same way, the second term of the bending energy φ_0^B reads

$$\varphi_0^B = 2\left(\frac{\partial^2 w}{\partial X^2} - Q^2 w \right)\frac{\partial^2 w}{\partial Y^2} - 2\left(\frac{\partial^2 w}{\partial X \partial Y} \right)^2 - 2Q^2\left(\frac{\partial w}{\partial Y} \right)^2. \tag{59}$$

As discussed in Damil and Potier-Ferry (2010), the derivatives of order three and order four in above differential equations can be neglected, since these high order derivatives may lead to spurious oscillations and the derivatives of order two are sufficient to recover the Ginzburg–Landau asymptotic approach. Consequently, this leads to the simplified macroscopic bending energy:

$$\mathbf{\Pi}_{ben}(w) = \frac{D_b}{2} \iint_{\Omega_f} \left\{ Q^4 w^2 - 2Q^2 w \Delta w + 4Q^2\left(\frac{\partial w}{\partial X} \right)^2 + 2(1 - \nu_f^2)Q^2\left[w\frac{\partial^2 w}{\partial Y^2} + \left(\frac{\partial w}{\partial Y} \right)^2 \right] \right\} \mathrm{d}\Omega. \tag{60}$$

The bending energy (60) that depends only on the envelope of the deflection can be expressed in the vector form:

$$\{\phi\} = {}^{t}\left\langle w, \frac{\partial w}{\partial X}, \frac{\partial w}{\partial Y} \right\rangle. \tag{61}$$

Note that the displacement vectors (49) and (61) are connected by a transform matrix $[\mathbf{T}_\phi]$, which reads

$$\{\phi\} = \left[\mathbf{T}_\phi\right]\{\theta\}, \tag{62}$$

where

$$[\mathbf{T}_\phi] = \begin{bmatrix} 0 & 0 & 0 & 0 & 1 & 0 & 0 \\ 0 & 0 & 0 & 0 & 0 & 1 & 0 \\ 0 & 0 & 0 & 0 & 0 & 0 & 1 \end{bmatrix}. \tag{63}$$

Consequently, the variational form of the bending energy can be written as

$$\delta\mathbf{\Pi}_{ben}(w) = \iint_{\Omega_f} \langle\delta\phi\rangle\left[\mathbf{L}_b\right]\{\phi\}\, \mathrm{d}\Omega, \tag{64}$$

in which

$$\left[\mathbf{L}_b\right] = 2D_b \begin{bmatrix} Q^4 & 0 & 0 \\ 0 & 6Q^2 & 0 \\ 0 & 0 & 2Q^2 \end{bmatrix}. \tag{65}$$

References

Allgower, E.L., Georg, K., 1990. Numerical Continuation Methods. Springer-Verlag, Berlin.

Audoly, B., Boudaoud, A., 2008a. Buckling of a stiff film bound to a compliant substrate. Part I. Formulation, linear stability of cylindrical patterns, secondary bifurcations. J. Mech. Phys. Solids 56, 2401–2421.

Audoly, B., Boudaoud, A., 2008b. Buckling of a stiff film bound to a compliant substrate. Part II. A global scenario for the formation of herringbone pattern. J. Mech. Phys. Solids 56, 2422–2443.

Audoly, B., Boudaoud, A., 2008c. Buckling of a stiff film bound to a compliant substrate. Part III. Herringbone solutions at large buckling parameter. J. Mech. Phys. Solids 56, 2444–2458.

Baguet, S., Cochelin, B., 2003. On the behaviour of the ANM continuation in the presence of bifurcations. Commun. Numer. Methods Eng. 19, 459–471.

Ben Dhia, H., 1998. Multiscale mechanical problems: the Arlequin method. C. R. Acad. Sci. Paris, Ser. IIb 326, 899–904.

Ben Dhia, H., Rateau, G., 2005. The Arlequin method as a flexible engineering design tool. Int. J. Numer. Methods Eng. 62, 1442–1462.

Boutyour, E.H., Zahrouni, H., Potier-Ferry, M., Boudi, M., 2004. Bifurcation points and bifurcated branches by an asymptotic numerical method and Padé approximants. Int. J. Numer. Methods Eng. 60, 1987–2012.

Bowden, N., Brittain, S., Evans, A.G., Hutchinson, J.W., Whitesides, G.M., 1998. Spontaneous formation of ordered structures in thin films of metals supported on an elastomeric polymer. Nature 393, 146–149.

Brau, F., Vandeparre, H., ASabbah, A., APoulard, C., Boudaoud, A., Damman, P., 2011. Multiple-length-scale elastic instability mimics parametric resonance of nonlinear oscillators. Nat. Phys. 7, 56–60.

Cai, S., Breid, D., Crosby, A.J., Suo, Z., Hutchinson, J.W., 2011. Periodic patterns and energy states of buckled films on compliant substrates. J. Mech. Phys. Solids 59, 1094–1114.

Cai, Z., Fu, Y., 1999. On the imperfection sensitivity of a coated elastic half-space. Proc. R. Soc. A 455, 3285–3309.

Cai, Z., Fu, Y., 2000. Exact and asymptotic stability analyses of a coated elastic half-space. Int. J. Solids Struct. 37, 3101–3119.

Cao, Y., Hutchinson, J.W., 2012a. Wrinkling phenomena in neo-Hookean film/substrate bilayers. J. Appl. Mech. 79, 031019-1–031019-9.

Cao, Y., Hutchinson, J.W., 2012b. From wrinkles to creases in elastomers: the instability and imperfection-sensitivity of wrinkling. Proc. R. Soc. A 468, 94–115.

Cao, Y., Jia, F., Zhao, Y., Feng, X., Yu, S., 2012. Buckling and post-buckling of a stiff film resting on an elastic graded substrate. Int. J. Solids Struct. 49, 1656–1664.

Chen, X., Hutchinson, J.W., 2004. Herringbone buckling patterns of compressed thin films on compliant substrates. J. Appl. Mech. 71, 597–603.

Cochelin, B., 1994. A path-following technique via an asymptotic-numerical method. Comput. Struct. 53, 1181–1192.

Cochelin, B., Damil, N., Potier-Ferry, M., 1994. Asymptotic-numerical Methods and Padé approximants for non-linear elastic structures. Int. J. Numer. Methods Eng. 37, 1187–1213.

Cochelin, B., Damil, N., Potier-Ferry, M., 2007. Méthode asymptotique numérique. Hermès Science Publications, Paris.

Cochelin, B., Medale, M., 2013. Power series analysis as a major breakthrough to improve the efficiency of Asymptotic Numerical Method in the vicinity of bifurcations. J. Comput. Phys. 236, 594–607.

Damil, N., Potier-Ferry, M., 1990. A new method to compute perturbed bifurcation: application to the buckling of imperfect elastic structures. Int. J. Eng. Sci. 28, 943–957.

Damil, N., Potier-Ferry, M., 2006. A generalized continuum approach to describe instability pattern formation by a multiple scale analysis. C. R. Mec. 334, 674–678.

Damil, N., Potier-Ferry, M., 2008. A generalized continuum approach to predict local buckling patterns of thin structures. Eur. J. Comput. Mech. 17, 945–956.

Damil, N., Potier-Ferry, M., 2010. Influence of local wrinkling on membrane behaviour: a new approach by the technique of slowly variable Fourier coefficients. J. Mech. Phys. Solids 58, 1139–1153.

Damil, N., Potier-Ferry, M., Hu, H., 2013. New nonlinear multi-scale models for wrinkled membranes. C. R. Mec. 341, 616–624.

Damil, N., Potier-Ferry, M., Hu, H., 2014. Membrane wrinkling revisited from a multi-scale point of view. Adv. Model. Simul. Eng. Sci. 1, 6.

Doedel, E., 1981. AUTO: A program for the automatic bifurcation analysis of autonomous systems. Congr. Numer. 30, 265–284.

Dowaikh, M.A., Ogden, R.W., 1990. On surface waves and deformations in a pre-stressed incompressible elastic solid. IMA J. Appl. Math. 44, 261–284.

Efimenko, K., Rackaitis, M., Manias, E., Vaziri, A., Mahadevan, L., Genzer, J., 2005. Nested self-similar wrinkling patterns in skins. Nat. Mater. 4, 293–297.

Hayes, M.A., Rivlin, R.S., 1961. Surface waves in deformed elastic materials. Arch. Ration. Mech. Anal. 8, 358–380.
Howarter, J.A., Stafford, C.M., 2010. Instabilities as a measurement tool for soft materials. Soft Matter 6, 5661–5666.
Huang, R., Im, S., 2006. Dynamics of wrinkle growth and coarsening in stressed thin films. Phys. Rev. E 74, 026214-1–026214-12.
Huang, Z.Y., Hong, W., Suo, Z., 2005. Nonlinear analyses of wrinkles in a film bonded to a compliant substrate. J. Mech. Phys. Solids 53, 2101–2118.
Iooss, G., Mielke, A., Demay, Y., 1989. Theory of steady Ginzburg–Landau equation in hydrodynamic stability problems. Eur. J. Mech. B-Fluid 8, 229–268.
Landau, L.D., Lifshitz, E.M., 1959. In: Theory of ElasticityPergamon, London.
Liu, Y., Yu, K., Hu, H., Belouettar, S., Potier-Ferry, M., Damil, N., 2012. A new Fourier-related double scale analysis for instability phenomena in sandwich structures. Int. J. Solids Struct. 49, 3077–3088.
Mahadevan, L., Rica, S., 2005. Self-organized origami. Science 307, 1740.
Medale, M., Cochelin, B., 2009. A parallel computer implementation of the Asymptotic Numerical Method to study thermal convection instabilities. J. Comput. Phys. 228, 8249–8262.
Mhada, K., Braikat, B., Damil, N., 2013. A 2D Fourier double scale analysis of global–local instability interaction in sandwich structures. In: Proceedings of 21ème Congrès Français de Mécanique, Bordeaux, France.
Mhada, K., Braikat, B., Hu, H., Damil, N., Potier-Ferry, M., 2012. About macroscopic models of instability pattern formation. Int. J. Solids Struct. 49, 2978–2989.
Newell, A., Whitehead, J., 1969. Finite band width, finite amplitude convection. J. Fluid Mech. 38, 279–303.
Rogers, J.A., Someya, T., Huang, Y., 2010. Materials and mechanics for stretchable electronics. Science 327, 1603–1607.
Shield, T.W., Kim, K.S., Shield, R.T., 1994. The buckling of an elastic layer bonded to an elastic substrate in plane strain. J. Appl. Mech. 61, 231–235.
Song, J., Jiang, H., Liu, Z.J., Khang, D.Y., Huang, Y., Rogers, J.A., Lu, C., Koh, C.G., 2008. Buckling of a stiff thin film on a compliant substrate in large deformation. Int. J. Solids Struct. 45, 3107–3121.
Steigmann, D., Ogden, R.W., 1997. Plane deformations of elastic solids with intrinsic boundary elasticity. In: Proc. R. Soc. A 453, 853–877.
Stoop, N., Lagrange, R., Terwagne, D., Reis, P.M., Dunkel, J., 2015. Curvature-induced symmetry breaking determines elastic surface patterns. Nat. Mater. 14, 337–342.
Sun, J.Y., Xia, S., Moon, M.W., Oh, K.H., Kim, K.S., 2012. Folding wrinkles of a thin stiff layer on a soft substrate. In: Proc. R. Soc. A 468, 932–953.
Vannucci, P., Cochelin, B., Damil, N., Potier-Ferry, M., 1998. An asymptotic-numerical method to compute bifurcating branches. Int. J. Numer. Methods Eng. 41, 1365–1389.
Wesfreid, J.E., Zaleski, S., 1984. Cellular structures in instabilities. Lecture Notes in Physics, vol. 210. Springer-Verlag, Heidelberg.
Xu, F., 2014. Numerical Study of Instability Patterns of Film-substrate Systems (Ph.D. thesis). Université de Lorraine, France.
Xu, F., Hu, H., Potier-Ferry, M., Belouettar, S., 2014a. Bridging techniques in a multi-scale modeling of pattern formation. Int. J. Solids Struct. 51, 3119–3134.
Xu, F., Koutsawa, Y., Potier-Ferry, M., Belouettar, S., 2015a. Instabilities in thin films on hyperelastic substrates by 3D finite elements. Int. J. Solids Struct. 69-70, 71–85.
Xu, F., Potier-Ferry, M., Belouettar, S., Cong, Y., 2014b. 3D finite element modeling for instabilities in thin films on soft substrates. Int. J. Solids Struct. 51, 3619–3632.
Xu, F., Potier-Ferry, M., Belouettar, S., Hu, H., 2015b. Multiple bifurcations in wrinkling analysis of thin films on compliant substrates. Int. J. Nonlinear Mech. 76, 203–222.
Zang, J., Zhao, X., Cao, Y., Hutchinson, J.W., 2012. Localized ridge wrinkling of stiff films on compliant substrates. J. Mech. Phys. Solids 60, 1265–1279.